Numerical Modelling of Detonation Initiation via Shock Interaction with Multiple Flames

Georgios Bakalis

A Thesis

in

The Department

of

Mechanical, Industrial and Aerospace Engineering

Presented in Partial Fulfillment of the Requirements

for the Degree of Master of Applied Science (Mechanical Engineering) at

Concordia University

Montreal, Quebec, Canada

December 2018

CONCORDIA UNIVERSITY
School of Graduate Studies

This is to certify that the thesis prepared

By: Georgios Bakalis

Entitled: Numerical Modelling of Detonation Initiation via Shock Interaction with Multiple Flames

and submitted in partial fulfillment of the requirements for the degree of

Master of Applied Science (Mechanical Engineering)

complies with the regulations of the University and meets the accepted standards with respect to originality and quality.

Signed by the final examining committee:

Chair
Dr. Carole El Ayoubi

Examiner
Dr. Lyes Kadem

Examiner
Dr. Nizar Bouguila

Thesis Supervisor(s)
Dr. Hoi Dick Ng

Approved by
Chair of Department or Graduate Program Director

Dean,

Date December 10, 2018

Abstract

Numerical Modelling of Detonation Initiation via Shock Interaction with Multiple Flames

Georgios Bakalis

Detonation in gaseous mixtures is a phenomenon of great importance for explosion safety assessment in hydrogen economy and for the development of advanced detonation-based propulsion systems. In practical applications, a detonation is generally caused by a deflagration to detonation transition (DDT) since a smaller amount of energy is required compared to a direct initiation. The key issue of DDT is finding the appropriate mechanisms to rapidly generate the detonation waves with a relatively weak ignition source. The objective of this work is to study numerically the possibility of DDT resulting from shock-multiple cylindrical flames interaction. The numerical setup aims to mimic an array of laminar flames ignited at different spark times, artificially inducing chemical activity to stimulate the coupling between the gasdynamics and the chemical energy release for the transition of deflagration-to-detonation. Using numerical simulations, a number of physical parameters are varied to determine their effect on the run-up distance as well as the time until the onset of detonation occurs, and to explore any scaling relationship among different them. The two-dimensional Navier-Stokes equations with one-step Arrhenius chemistry including the effects of viscosity, thermal conduction and molecular diffusion are used for the simulations. For comparison, simulations with Euler equations are also performed. The finite-volume operator splitting scheme used is based on the 2nd order Godunov-type, Weighted Average Flux (WAF) method with an approximate HLLC Riemann Solver. An Adaptive Mesh Refinement (AMR) technique is used to increase the resolution in areas of interest. The simulation results show that the interaction of the weak shock with the first cylindrical flame demonstrates very good agreement with the results in the literature and that a single weak shock–flame interaction was not enough to cause prompt DDT. However, a high degree of Richtmyer-Meshkov instabilities induced by repeated shock-flame interactions along with shock-boundary interactions generate turbulence that accelerates the flame brush, until eventually a hot spot ignition in the unreacted material develops into a multi-headed detonation wave. The simulation results also show that DDT is sensitive to the simulation method and that certain simulation parameters significantly affect the DDT phenomenon.

Acknowledgements

I would like to thank my supervisor Dr. Hoi Dick Ng for introducing me to this research field, for all the guidance he provided me for this Thesis and for motivating me to further continue my research in this field. I would also like to express my deepest gratitude to my parents and my brother for their continuing support and encouragement in all these years of my studies.

Table of Contents

List of Figures

List of Tables

Glossary

ρ	Density (kg/m^3)
t	Time (s)
E	Total energy (J·kg/m^3)
p	Pressure (Pa)
D	Mass diffusion coefficient (m^2/s)
$\underline{\tau}$	Viscous stress tensor (Pa)
Q	Energy release rate (J/kg)
λ	Reaction progress
T	Temperature (K)
M	Molecular mass (g/mol)
R	Universal gas constant (8314 J / (kg·K))
$\mathbf{V}$	Fluid velocity, $\mathbf{V} = (u, v, w)$ (m/s)
ω	Arrhenius reaction rate (s^{-1})
E_A	Arrhenius activation energy (J)
ν	Kinematic viscosity coefficient (m^2/s)
D	Mass diffusion coefficient (m^2/s)
a	Thermal diffusivity (m^2/s)
c_k	Courant number
S	Wave speed (m/s)
L_x	Domain length (m)
L_y,	Domain height (mm)
r	Initial flame radius (mm)
M_o	Incident shock Mach number
l	Distance between discrete flames (mm)
γ	Ratio of specific heats, $\gamma = C_p/C_v$
Δx	Mesh spacing (μm)

l_2 Initial distance of the first flame kernel from the left boundary (mm)

l_1 Initial distance between the incident shock and the left boundary (mm)

f Overdriven factor

D Overdriven detonation velocity (m/s)

D_{cj} Chapman-Jouguet detonation velocity (m/s)

Chapter 1

Introduction

A gaseous detonation is a supersonic combustion-driven wave travelling at a velocity of the order of 2 km/s, across which a significant pressure and temperature increase occur in the medium. Its initiation and propagation require strong non-linear coupling between a shock wave and energy release through chemical reactions (Fickett & Davis 1979). This combustion phenomenon is of broad interest to many safety engineering applications and industrial processes in the chemical and energy sectors, as well as the military research establishments. The ability to predict the detonation sensitivity of explosives, their initiation, and limits are critical to proper risk assessment of chemical facilities, mitigation of accidental explosions and the transportation safety of hazardous materials (Ng & Lee 2008). On the contrary this self-sustained, supersonic, combustion-driven wave is also turning into a viable option for the development of advanced propulsion systems which harness the conditions generated by this combustion mode to achieve a high thermal cycle efficiency (Kailasanath 2003; Wolanski 2013). An example is the concept of Pulse Detonation Engines (PDEs). These engines produce thrust with continuous short bursts and can be used for commercial, military and space flight purposes. Compared to jet engines they have higher efficiency and can operate at hypersonic speeds. The simple PDE design concepts do not have moving parts; therefore, they are deemed to be reliable and have lower maintenance costs (Roy et al. 2004). A schematic showing the operation of a PDE is shown in Figure 1.1.

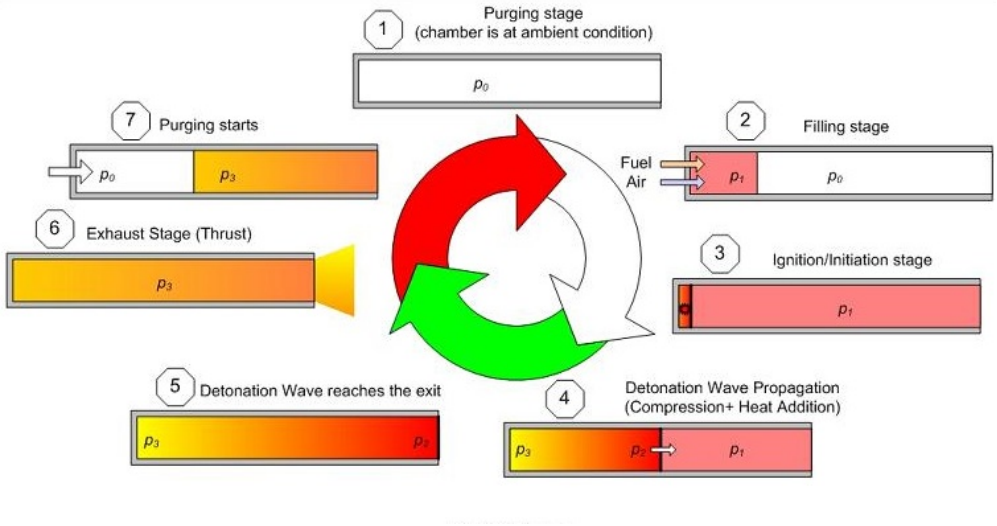

Figure 1.1 *PDE Cycle, retrieved from http://arc.uta.edu/research/pde.htm*

Many fundamental aspects of detonations can be found in the comprehensive monograph by Lee (2008). Other comprehensive discussions on recent detonation modeling can be found in recent reviews (Shepherd 2009; Oran 2015) and the Springer Volume edited by Zhang (2012). Nevertheless, these reviews illustrate that there are still outstanding problems in our understanding of detonations, one of it is the lack of quantitative descriptions of detonation initiation, and efficient mean to establish a detonation wave for practical applications.

1.1 Initiation of gaseous detonations

Generally, a detonation can be formed in two ways. One way is by a rapid deposition of a large amount of energy into the combustion mixture, referred to as direct initiation (Lee & Higgins 1999; Ng & Lee 2003). The detonation is formed instantaneously from the decay of the generated strong blast wave, as shown in Figure 1.2. In the limit of an ideal point source energy, the initiation energy becomes the sole parameter that determines the possible outcome of the initiation process, i.e., whether a detonation can be initiated or not. This method of detonation initiation requires the use of a very high energy deposition source, e.g., from a high-voltage capacity spark discharge, a condensed phase energetic explosive material, or laser ignition (Lee 1977). Hence, it is not a practical way for any realistic propulsion applications.

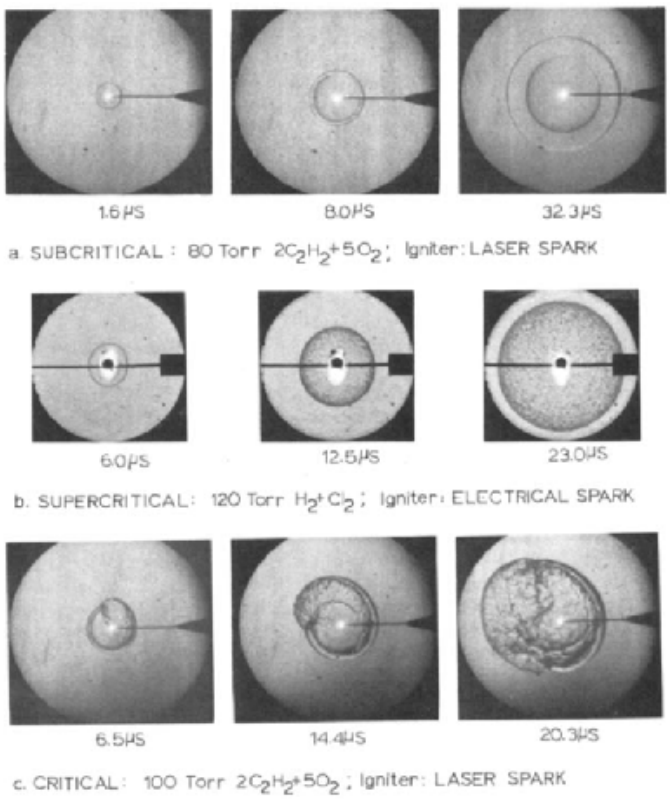

Figure 1.2 *Experimental results showing the successful and unsuccessful direct initiation of detonation. (Bach et al. 1969)*

The other mode of detonation initiation is referred to as deflagration to detonation transition (DDT). The Deflagration to Detonation Transition (DDT) is a phenomenon which attracts high research interest, with applications in propulsion (Roy et al. 2004) and process safety (Molkov 2012; Middha & Hansen 2008; Ciccarelli & Dorofeev 2008; Schultz et al. 1999). In fact, since direct initiation requires an extremely large energy deposition relative to deflagrative ignition (several orders of magnitude more), DDT phenomenon is the most probable cause resulting in the formation of detonations in accidental explosions and practically is perhaps the sole initiation scheme feasible in detonation-based engine applications. DDT involves an initial ignition of a combustible mixture by some relatively weak energy source producing a laminar flame, followed by an acceleration through interactions with its boundary. The generation of turbulence resulted into a coupled shock wave-reaction zone structure and eventually the onset of a detonation under appropriate conditions (Oran & Gamezo 2007). The distance required for the transition is referred

to as the DDT or “run-up” distance. The process is illustrated schematically in Fig. 1.3a and an experimental observation is given in Figure 1.3b.

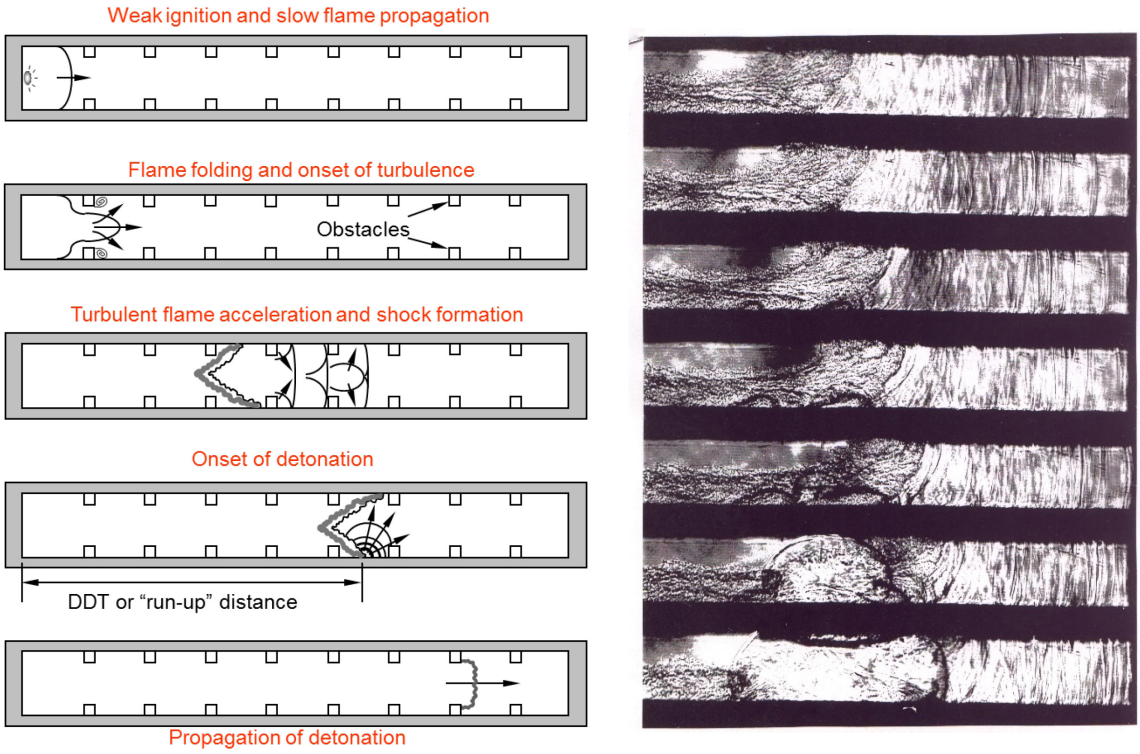

Figure 1.3 *Deflagration-to-detonation transition: a) a schematic illustration by Higgins et al. (2001); and b) experimental photographs by Urtiew & Oppenheim (1966)*

1.2 DDT process for detonation propulsion

For the successful and steady operation of detonation-based engines such as pulse detonation engines (PDE), repetitive initiation of detonation waves is required (Roy et al. 2004). The Deflagration to Detonation Transition is by nature a complicated and stochastic process due to the various turbulent and instability mechanisms that cause the transition, from low-speed flame propagation, to a high-speed turbulent deflagration and eventually a detonation wave; after a small spark has created a deflagration, the transition needs to cover a relatively very long process path for the onset of detonation. Experiments in simple straight tubes also showed that in the acceleration of a flame to a detonation, the transition or run-up distance required for

deflagration-to-detonation transition is highly irreproducible due to the array of turbulent and instability mechanisms that play a role in promoting transition to detonation (Lee 2008). Therefore, having consistent and repeatable DDT as a viable initiation method in detonation engine applications is challenging. The main research goals concerning these engines are to address the key issue of finding appropriate mechanisms for rapidly generating detonation waves from DDT with a relatively weak ignition source; in other words, to reduce the time and distance required for the DDT transition to occur in order to minimize the size of the engineering system, while minimizing the required energy and producing reproducible shot-to-shot performance (Roy et al. 2004; Schultz et al. 1999). Achieving these goals will result in more efficient, compact engines which can operate with increased pulse frequency. Up-to-date, the common techniques to facilitate the flame acceleration are to modify the boundary condition by inserting a Shchelkin spiral, rectangular obstacles or by using jets to promote the generation of turbulence.

In the literature, a number of computational studies on the initial shock-flame and boundary interactions have been performed to describe the fundamentals of DDT process (Oran & Gamezo 2007; Khokhlov et al. 1999; Khokhlov & Oran 1999; Gamezo et al. 2001). These studies show that compressible turbulence and shock-flame interaction are responsible to create the proper condition for the final onset of detonation. As in other detonation phenomena, the key mechanism in DDT for successful transition to detonation is the close coupling of energy release with the gasdynamic flow (Frolov 2006). In the pioneering work by Zel'dovich et al. (1970) the coupling originated from the shock-flame and shock-boundary interaction, eventually leading to a spontaneous onset of detonation is modeled by an initial gradient of auto-ignition delay time through temperature and composition non-uniformities in the pre-conditioned reactive mixture. Similar studies were subsequently carried out numerically and theoretically by a number of researchers, see Bartenev & Gelfand (2000) and references therein. These factors promote the amplification of a high-speed shock through the coherent energy release, later termed by Lee & Moen (1979) as the concept of Shock Wave Amplification by Coherent Energy Release (SWACER). The latter was used to qualitatively explain the photochemical initiation and turbulent jet initiation of gaseous detonations, 'explosion within the explosion' at the onset of detonation (Lee 2008) and detonation formation from a temperature gradient (Khokhlov et al. 1999; Kapila et al. 2002).

1.3 DDT enhancement using the concept of multiple sparks

In order to promote the coherent coupling between the gas dynamics and energy release to control the transition of deflagration to detonation, an engineering concept was previously proposed using spatially distributed energy release. The idea is to synchronize the propagation and amplification of a weak shock interacting with an array of laminar flames ignited through different spark sequences in the reactive mixture to achieve very short distances for DDT in smooth tubes. Such ideas of using external sources to facilitate the onset of a detonation was proposed as early as the 1950's by Zel'dovich & Kompaneets (1955) theoretically and has been applied experimentally, notably by Frolov et al. (2003, 2006) using controlled triggering of electric ignition, see Figure 1.4. The time delay of each ignition could be varied within a wide range (from 10 to 500 μs). The energy of discharges is controlled by the voltage ranging from 1500 to 2500 V. The experimental work by Frolov et al. (2003) has proved that the use of relatively weak igniters with optimally tuned triggering times can promote detonation initiation in premixed $C_3H_8 + O_2 + 3\ N_2$ and stoichiometric C_3H_8/Air mixtures at distances as short as 0.6–0.7 m in a 2-inch diameter tube at normal initial conditions (at about the cross section CS7 shown in Figure 1.4). Hu et al. (2010) also simulated the rapid detonation initiation by sparks modelled by a high-energy region with ignition temperature but also with high ignition pressure. These studies demonstrate that the initiation technique using multiple sparks has the potential to induce DDT.

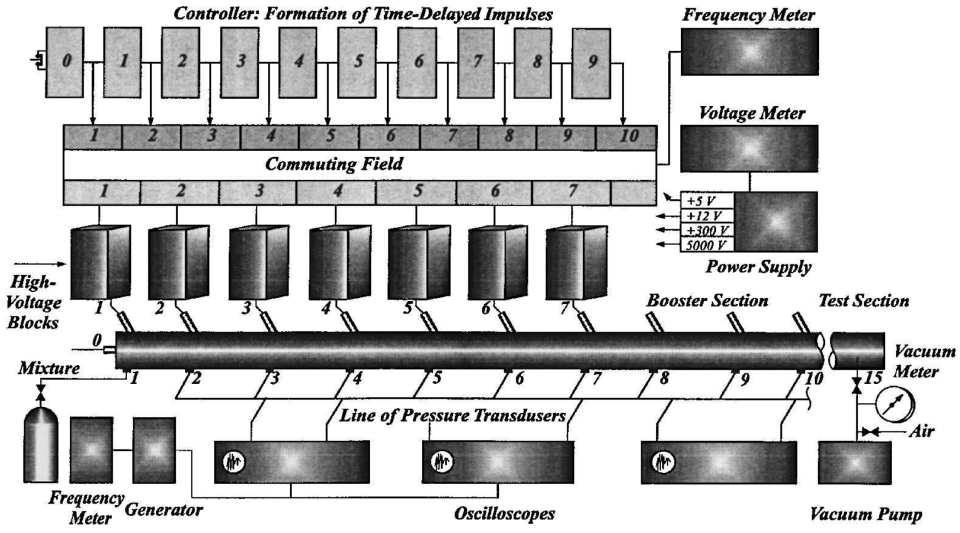

Figure 1.4 *Experimental detonation facility with controlled triggering of electric discharges used by Frolov et al. (2003, 2006)*

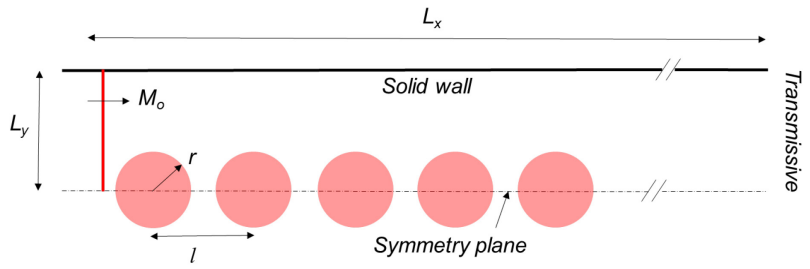

Figure 1.5 *Computational setup of the present problem*

1.4 Objective of the thesis

The objective of this work is to study numerically the possibility of deflagration-to-detonation transition resulting from shock-multiple flame interaction. In this numerical investigation, the phenomenon is described by a relatively weak shock wave travelling along a tube filled with a reactive mixture and an array of laminar flames ignited through different spark sequences as a means of artificially inducing chemical activity to stimulate the strong coupling required for the transition of deflagration-to-detonation. The present numerical work differs from that of Hu et al. (2010). The present investigation considers only weak sparks resulting only in the generation of laminar flame kernels across which the pressure remains constant. The pressure increase due to the high-voltage discharge, as in the experiments by Frolov et al. (2003) and in the simulation by Hu et al. (2010) are thus eliminated. The outcome of this numerical work will further solidify whether the proposed concept of using multiple weak sparks (while minimizing the input spark energy as much as possible) can be a potential approach for propulsion applications. Besides, the present investigation is an extension of Khokhlov et al. (1999) which analyzed the flow field resulting from the interaction between a weak shock and a single laminar kernel. The possibility of deflagration-to-detonation transition resulting from shock-multiple flames interaction – the scope of this thesis – has not been explored.

Using numerical simulations, a number of parameters are varied to determine their effect on the run-up distance and the time until the onset of detonation occurs. The shock wave amplification by coherent energy release (SWACER) mechanism and others fundamental gasdynamics interactions governing the phenomenon are investigated. As shown in many numerical studies, modelling DDT is highly sensitive to the numerical details of the simulation and thus gives the motivation of the present study to verify various numerical effect on the simulation results.

Numerical verifications were made on the shock-multiple flame interaction and subsequent DDT and how these processes depend on the numerics.

1.5 Thesis outline

Current chapter of the thesis introduces the basic concepts and related literature review of the subject matter. The methodology used in the present investigation is numerical simulations, Chapter 2 is thus devoted to the detailed description of the numerical method and its validation for reactive compressible flow simulations. Chapters 3 and 4 present the numerical simulations and analyze the flow field from the DDT process, in an extensive parametric fashion. Final chapter is the conclusions and recommendations of future work.

Chapter 2

Problem Formulation and Numerical Method

The methodology used in the present investigation is numerical simulations. It is thus important to describe the mathematical model and assess the numerical technique used for the present simulation, which involves many aspects of the compressible flow with shock dynamics. This chapter is therefore devoted to the detailed description of the governing equations and the numerical method to seek approximate solutions of the governing equations. To demonstrate its robustness and accuracy, the numerical scheme is assessed via the benchmark shock tube tests.

2.1 Mathematical model

The reactive flow that was studied in this thesis is governed by the unsteady, multi-dimensional reactive Navier-Stokes equations:

$$\frac{\partial \rho}{\partial t} + \nabla \cdot (\rho \boldsymbol{V}) = 0$$

$$\frac{\partial (\rho \boldsymbol{V}_i)}{\partial t} + \nabla \cdot (\rho \boldsymbol{V}_i \boldsymbol{V}) + \frac{\partial p}{\partial x_i} = \nabla \cdot \tau_i$$

$$\frac{\partial E}{\partial t} + \nabla\big((E + p) \cdot \boldsymbol{V}\big) = \nabla(k \nabla T) + \nabla \cdot \big(\underline{\tau} \boldsymbol{V}\big) + \dot{\omega} Q$$

$$\frac{\partial \rho \lambda}{\partial t} + \nabla \cdot (\rho \lambda \boldsymbol{V}) = \nabla \cdot (\rho D \nabla \lambda) - \dot{\omega}$$

where $\mathbf{V} = (u, v, w)$ is the particle velocity vector, ρ the density, E is the total energy, p the pressure, k the thermal conductivity, D the mass diffusion coefficient, $\underline{\tau}$ the viscous stress tensor, i.e., $\tau_{i,j} = \rho v \left(\frac{\partial \mathbf{V}_i}{\partial x_j} + \frac{\partial \mathbf{V}_j}{\partial x_i} \right)$ where v is the kinematic viscosity coefficient. For the chemistry part, Q

is the chemical energy release into the system per unit mass of reactant converted and λ the local concentration of reactant across the domain with $\lambda = 1$ for unreacted material and $\lambda = 0$ for reacted products. The reactive component of the flow is modeled by the last equation, along with the source term $\dot{\omega}Q$ in the energy equation. The reactive medium is modelled as a single-gas approximation with constant specific heat ratio γ and behaves as an ideal gas with the equation of state:

$$T = \frac{pM}{\rho R}$$

where T is the temperature, M the molecular weight and R the universal gas constant, respectively. The total energy is thus expressed as:

$$E = \frac{p}{(\gamma - 1)} + \frac{1}{2}\mathbf{V} \cdot \mathbf{V}$$

A single step reaction model is used, in which the reactants are considered to convert directly to products, without intermediate (chain branching or other) reactions. The reaction rate is given by:

$$\dot{\omega} = A \cdot \rho \cdot \lambda exp\left(\frac{-E_A}{RT}\right)$$

where A is a pre-exponential factor and E_A is the activation energy of the system. The transport coefficients, i.e., viscosity ν, mass diffusivity D, and thermal diffusivity $a = k/\rho c_p$, where k is the thermal conductivity, vary with temperature according to:

$$\nu = \nu_o \frac{T^n}{\rho} \qquad D = D_o \frac{T^n}{\rho} \qquad \alpha = \alpha_o \frac{T^n}{\rho}$$

The parameters ν_o, D_o, and α_o are assumed to be constant, and n is a constant exponent. It is worth noting that this type of flow model has been used in past work for acetylene, ethylene, and hydrogen to solve a variety of combustion and detonation problems involving shock–flame interactions and to compute the properties of the cellular structure of detonations, e.g., Khokhlov et al. (1999), Gamezo et al. (2001); Oran and Gamezo (2007); Oran (2015); Kessler et al. (2010), etc.

2.2 Description of the numerical method

The full unsteady reactive Navier-Stoke equations are described by a set of partial differential equations and must be solved numerically using some reliable numerical method. These unsteady governing equations describing the dynamics of the reactive flow indeed express a system of hyperbolic conservation laws with additional source terms account for the chemical reactions and diffusions.

2.2.1. Operator splitting

For a system of equations where except for advection there is also diffusion and a reactive source, the system can be written in operator form as:

$$\frac{\partial}{\partial t}U = \mathbb{A}(U) + \mathbb{R}(U) + \mathbb{D}(U)$$

where $\mathbb{A}$ is the advection operator, $\mathbb{R}$ is the reactive source operator and $\mathbb{D}$ is the diffusion operator. In an operator splitting scheme the time-step Δt is assumed to be sufficiently small, thus allowing each operator to be applied independently of the others:

$$\bar{U}^{(1)} = \bar{U}^{t} + \Delta t A(\bar{U}^{t})$$

$$\bar{U}^{(2)} = \bar{U}^{(1)} + \Delta t R\left(\bar{U}^{(1)}\right)$$

$$\bar{U}^{t+\Delta t} = \bar{U}^{(2)} + \Delta t D\left(\bar{U}^{(2)}\right)$$

where A, R, D are the discrete versions of the respective operators above. Because second order of accuracy is required, Strang's fractional step operator splitting approach is being used, which can be described by the following steps:

$$\bar{U}^{ad} = \bar{U}^{t} + \frac{\Delta t}{2} A(\bar{U}^{t})$$

$$\bar{U}^{di} = \bar{U}^{ad} + \frac{\Delta t}{2} D(\bar{U}^{ad})$$

$$\bar{U}^{re} = \bar{U}^{di} + \Delta t R\left(\bar{U}^{di}\right)$$

$$\bar{U}^{di'} = \bar{U}^{re} + \frac{\Delta t}{2} D(\bar{U}^{re})$$

$$\bar{U}^{t+\Delta t} = \bar{U}^{di'} + \frac{\Delta t}{2} A\left(\bar{U}^{di'}\right)$$

Additionally, for the present problem in 2-D Cartesian coordinates, the convective part given by the Euler equations can be written in the form:

$$PDE: U_t + F(U)_x + G(U)_y = 0$$

$$IC: U(x, y, t^n) = U^n$$

where U is the vector of conserved variables and $F(U)$ and $G(U)$ the fluxes in the x and y directions. To solve these equations, a similar approach of dimensional splitting can be used. In this approach, one dimensional methods are applied in each coordinate direction. The simplest version of the approach replaces the above initial value problem (IVP) by a sequence of IVPs, in which the flux is considered in one direction at a time:

$$\left.\begin{matrix} PDEs: U_t + F(U)_x = 0 \\ ICs: U^n \end{matrix}\right\} \rightarrow U^{n+\frac{1}{2}}$$

$$\left.\begin{matrix} PDEs: U_t + G(U)_y = 0 \\ ICs: U^{n+\frac{1}{2}} \end{matrix}\right\} \rightarrow U^{n+1}$$

While the viscous, heat, and diffusion (Navier-Stokes) terms are actually a system of ODEs which can be evaluated using a standard second-order finite differencing, the Euler fluxes are needed to be evaluated by solving a Riemann problem at cell interfaces using a dedicated hyperbolic solver.

2.2.2 Weighted Average Flux (WAF) scheme

A variety of efficient high-resolution numerical schemes for hyperbolic systems of partial differential equations has been devised in the recent years. Many of these modern high-resolution numerical schemes are often based on upwind differencing, which are generally most suitable for the numerical solution of systems of hyperbolic conservation laws as they introduce characteristic information regarding the local directionality of the flow along the discontinuous interfaces of the spatial cells. These upwind differencing schemes generally require the solution of the corresponding local Riemann problem to evaluate the flux terms at the cell interfaces and this in turn greatly complicates the upwind algorithm (Toro 2006). Beside the exact analytical solutions, various methods exist to efficiently calculate approximate solutions to this Riemann problem, such as the HLLC, Roe-Pike or Osher solvers, and again details of these can be found in (Toro 2006).

In this thesis, the method employed is that of the approximate HLLC solver which will be described in the following section.

In the context of reactive flow studies, a full description of the phenomena requires reliable and highly resolved numerical simulations. In this work, a well-established high-resolution upwind scheme, namely the Weighted Average Flux (WAF) scheme by Toro is considered in this investigation (Toro 2006; Toro & Billet 2000). This scheme is chosen for its ability to resolve shocks and contact surfaces over a very small number of cells and its very low numerical diffusion. This particular numerical scheme has also been used successfully in many other detonation studies (Nikiforakis & Clarke 1996a,b; Bates 2005; Kindracki et al. 2011).

The WAF method is a second-order extension of the Godunov scheme. Consider first a 1-D system of partial differential equations written in conservative form,

$$U_t + F(U)_x = 0$$

where U is the vector of conserved variables and $F(U)$ the convective fluxes. The resulting update finite volume formula derived by considering the equivalent integral formulation,

$$\oint [Udx + F(U)dt] = 0$$

can be written as:

$$u_i^{n+1} = u_i^n + \frac{\Delta t}{\Delta x}\left[F_{i-\frac{1}{2}} - F_{i+\frac{1}{2}}\right]$$

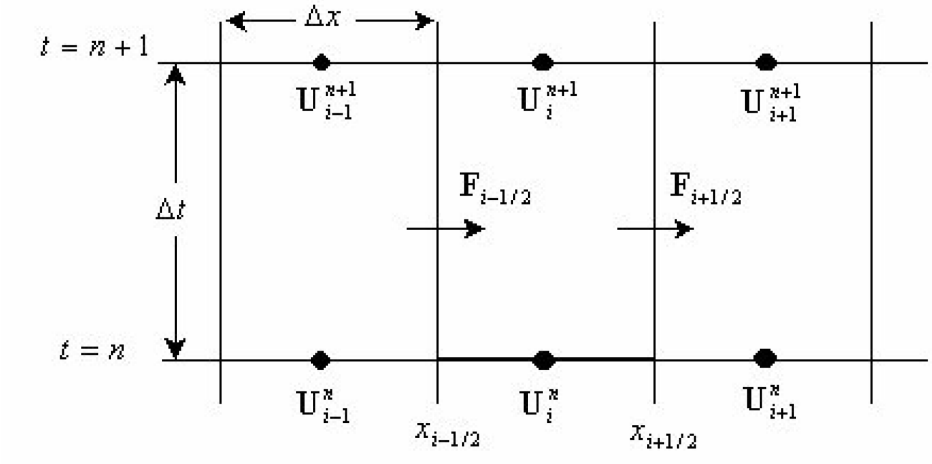

Figure 2.1 *Discretized domain for computation*

The resulting formulation can be represented as the discretized domain given in Figure 2.1. As with Godunov's scheme, the WAF method solves the two local Riemann problems $RP\ (u_{i-1}, u_i)$ and $RP\ (u_i, u_{i+1})$ to obtain the intercell fluxes $F_{i-\frac{1}{2}}$ and $F_{i+\frac{1}{2}}$ and uses the above equation to calculate the values at the next step. However, the key difference is that the WAF method computes the intercell flux the Riemann problem with data u_i and u_{i+1} at half the time step, instead of one time-step Δt, as can be seen in Figure 2.2.

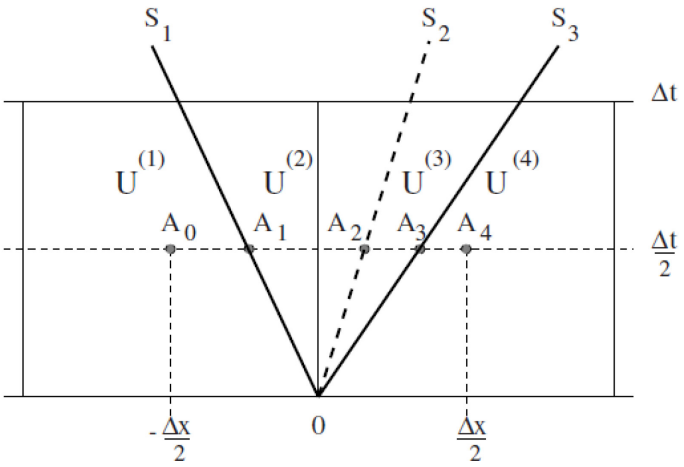

Figure 2.2 *Waves and constant states considered in WAF method*

In Fig. 2.2 it can be seen that this method considers three waves of speeds S1, S2 and S3 that separate four constant states: $u_i, u_{*L}, u_{*R}, u_{i+1}$. The middle wave is always a contact discontinuity, whereas the right and left waves can be either shock or rarefaction waves. The WAF intercell flux is represented by an integral average of the physical flux across the full structure of the solution of a local Riemann problem.

$$F_{i+1/2} = \frac{1}{\Delta x}\int_{-\Delta x/2}^{\Delta x/2} F\left(U_{i+\frac{1}{2}}\left(x, \frac{\Delta t}{2}\right)\right) dx$$

Since the states between waves are constant, the integral average becomes summation of the fluxes at each constant state with weight determined by the respective wave speeds, plus integrals of the fluxes across any rarefaction waves present. However, for practical purposes, the flux can be estimated by approximating the state across the rarefaction wave to be that closest to $x = 0$ within the wave. Hence the integral simplifies to a sum over waves,

$$F_{i+1/2} = \sum_{k=1}^{N+1} W_k \cdot F_{i+1/2}^{(k)}$$

where $F_{i+1/2}^{(k)} = F\left(U^{(K)}\right)$, N is the number of waves and W_k , $k = 1 - 4$, are the normalized lengths of the segments A_0A_1, A_1A_2, A_2A_3, A_3A_4, referred to as weights. These weights can be computed from the Courant number as:

$$W_k = \frac{1}{2}(c_K - c_{K-1}) \, , c_0 = -1 \; and \; c_{N+1} = 1$$

The Courant numbers c_k associated with the wave k of speed S_K, can be calculated from:

$$c_K = \frac{\Delta t \cdot S_K}{\Delta x}$$

Substituting $\underline{W}_k$ into the integral average gives an alternative form for the WAF flux:

$$F_{i+1/2} = \frac{1}{2}(F_i + F_{i+1}) - \frac{1}{2}\sum_{k=1}^{N} c_K \cdot \Delta F_{i+1/2}^{(k)}$$

where $\Delta F_{i+1/2}^{(k)} = F_{i+1/2}^{(k+1)} - F_{i+1/2}^{(k)}$ is the flux jump across wave K of CFL number C_K. This derived scheme is second order accurate, therefore from Godunov's theorem it cannot be monotone, and spurious oscillations will occur at large gradients (e.g. at shocks).

2.2.3 Total Variation Diminishing (TVD) version of WAF

To avoid spurious oscillations appear in the vicinity of a high gradient, an extended WAF version was used in this thesis to ensure the scheme satisfies the Total Variation Diminishing condition, known as TVD version of the WAF method, in which the wave speeds are limited by a limiting function Φ (Toro 2006). This flux limiter allows the scheme to switch between higher order and first order schemes. Therefore, an increased accuracy is achieved, and the creation of spurious oscillations is avoided in areas of discontinuity or high-gradient. The flux for the TVD WAF method with limiter function $\Phi_{i+1/2}^{(k)}$ is given by:

$$F_{i+1/2} = \frac{1}{2}(F_i + F_{i+1}) - \frac{1}{2}\sum_{k=1}^{N} sign(C_K) \cdot \Phi_{i+1/2}^{(k)} \cdot \Delta F_{i+1/2}^{(k)}$$

where $\Phi_{i+1/2}^{(k)} = \Phi_{i+\frac{1}{2}}(r_{i+\frac{1}{2}}^{(k)})$ is a limiter function and the flow parameter $r_{1+1/2}$ is the ratio of the upwind change in the flow to the local change:

$$r_{i+1/2}^{(k)} = \begin{cases} \dfrac{\Delta q_{i-1/2}^{(k)}}{\Delta q_{i+1/2}^{(k)}} \,, if\ c_k > 0 \\ \dfrac{\Delta q_{i+3/2}^{(k)}}{\Delta q_{i+1/2}^{(k)}} \,, if\ c_k < 0 \end{cases}$$

Δq is the change in some function of the flow variables across the wave, indicating the "strength" of the wave. For Euler equations, the chosen flow variable to calculate the flow jumps $\Delta q_{i+1/2}$ is usually density ($q = \rho$). For smooth parts of the solution, the flow function will be equal to 1. For TVD WAF, many flux limiters are available, e.g., MINBEE, SUPERBEE, Van Leer, etc. In this work, van Leer limiter is chosen as given by:

$$\Phi(|c|\,, r) = \begin{Bmatrix} 1 & if\ r \le 0 \\ 1 - \dfrac{2(1-|c|)r}{1+r} & if\ r > 0 \end{Bmatrix}$$

To calculate the intercell flux $F_{i+1/2}$, the $F_{i+1/2}^{(k)}$ fluxes and wave speeds S_K must be known. These can be found either by the exact solution of the Riemann problem or by approximations to the exact solution (approximate Riemann solvers such as HLL, HLLC, etc.) for a pair of initial data states (U_i^n, U_{i+1}^n). By regarding the numerical solution U_i^n to be piecewise constant across each cell, the Riemann problem can be solved at time $t = \Delta t$ with initial conditions $U_i^n$and U_i^{n+1} to obtain the solution at $U_{i+1/2}^n$, which can then be used to compute $F_{i+1/2}^n$ and then to obtain the WAF fluxes at every cell boundary for the computation of U_i^{n+1}.

2.2.4. Approximate HLLC Riemann Solver

The Riemann problem for a set of hyperbolic conservation laws deals with the solution for $t > 0$ with initial conditions discontinuous at the origin, i.e.,

$$U(x,0) = U^{(0)}(x) = \begin{cases} U_L \; if \; x \leq 0 \\ U_R \; if \; x > 0 \end{cases}$$

The structure of the Riemann problem for the Euler equations consists of three wave families, corresponding to the eigenvalues $\lambda_1 = u - a$, $\lambda_2 = u$ and $\lambda_3 = u + a$, as can be seen in Figure 2.3. The central wave is always a contact discontinuity, the left and right waves can be either a rarefaction wave or a shock wave.

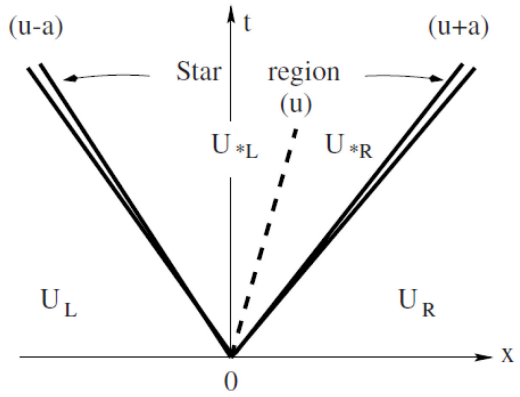

Figure 2.3 *Wave structure for the solution of the 1-D Euler Riemann problem in the x-t plane*

For the purpose of directly computing numerical fluxes, approximate technique is developed for solving the Riemann problem approximately and the resulting algorithms have been known as Harten, Lax and van Leer (HLL) approximate Riemann solvers. Unlike the analytical approach to solve the exact Riemann problem giving a vast amount of information, which is time consuming, approximate Riemann Solver gives an approximation for the intercell numerical flux directly, and the differences in result are generally negligible. The HLL Riemann solver assumes a single constant state between two nonlinear waves (shock or rarefaction) and requires estimates for the fastest signal velocities emerging from the initial discontinuity at the interface, resulting in a the two-wave model for the solution structure of the problem. The HLLC scheme used in this work is a modification of the HLL scheme wherein the missing contacts and shear waves are put back into

the structure of the approximate solver. The HLLC scheme provides a more accurate approach with a three-wave model, preserving the solution structure with shock, contact, and shear waves.

To compute wave speeds of the left-going and right-going waves S_L, S_R, the pressure-velocity based wave estimations presented by Toro (2006) are used to estimate the shock and the rarefaction waves accurately. The pressure in the star region is estimated using:

$$p_* = \max(0, p_{pvrs})$$

$$p_{pvrs} = \frac{1}{2}(p_L + p_R) - \frac{1}{2}(u_R - u_L)\bar{\rho}\bar{\alpha}$$

$$\bar{\rho} = \frac{1}{2}(\rho_L + \rho_R)\,, \bar{a} = \frac{1}{2}(a_L + a_R)$$

The wave speed estimates can then be calculated with:

$$S_L = u_L - a_L q_L\,, S_R = u_R + a_R q_R$$

$$q_K = \begin{Bmatrix} 1 & if\ p_* \le p_K \\ \left[1 + \frac{\gamma+1}{2\gamma}\left({}^{p_*}/_{p_K} - 1\right)\right]^{1/2} & if\ p_* > p_K \end{Bmatrix}$$

An estimate for the speed of the contact surface was restored in Toro *et al.* (1994) in term of the S_L and S_R to form the HLLC solver. The speed S^* of the middle wave is derived as:

$$S_* = \frac{p_R - p_L + \rho_L u_L(S_L - u_L) - \rho_R u_R(S_R - u_R)}{\rho_L(S_L - u_L) - \rho_R(S_R - u_R)}$$

which together with an estimated “star state" between the left and rightmost waves

$$U_{*K} = \rho_K \left(\frac{S_k - u_K}{S_K - S_*}\right) \begin{bmatrix} 1 \\ S_* \\ v_K \\ w_K \\ \frac{E_K}{\rho_K} + (S_* - u_K)\left[S_* + \frac{p_K}{\rho_K(S_K - u_K)}\right] \end{bmatrix}$$

allows for the simple expression of the HLLC flux between two cells,

$$F_{i+\frac{1}{2}}^{HLLC} = \begin{cases} F(U_L) & 0 \le S_L \\ F_{*L} = F(U_L) + S_L(U_{*L} - U_L) & S_L \le 0 \le S_* \\ F_{*R} = F(U_R) + S_R(U_{*R} - U_R) & S_* \le 0 \le S_R \\ F(U_R) & S_R \le 0 \end{cases}$$

By applying the WAF scheme directly to the HLLC approximate Riemann solver, the numerical flux at the interface boundary can be written as:

$$F_{i+\frac{1}{2}}^{HLLC,WAF} = \frac{1}{2}(F_L + F_R) - \frac{1}{2}\begin{bmatrix} sign(C_1)\cdot\Phi^{(1)}\cdot(F_{*L} - F_L) \\ sign(C_2)\cdot\Phi^{(2)}\cdot(F_{*R} - F_{*L}) \\ sign(C_3)\cdot\Phi^{(3)}\cdot(F_R - F_{*R}) \end{bmatrix}$$

2.3 Adaptive Mesh Refinement (AMR)

For reactive flow simulations, it is often necessary having high resolutions in order to ensure that detailed features within the reactive flow structure are properly resolved. However, the use of very small time steps and uniform fine grid of cells in a long computational domain requires a much larger amount of computer resources. For reactive flow problems, high resolutions are in fact only needed in part of the computational domain as most reactions are often completed in a narrow, localized region. It is thus more economical to refine only in this region and use coarser resolutions elsewhere, hence reducing the computational demands without sacrificing accuracy.

The adaptive mesh refinement (AMR) technique originally developed by Berger & Oliger (1984) allows the mesh resolution to dynamically increase in specific areas of the domain, where improved resolution is required to resolve developing features, while leaving less interesting parts of the domain at lower resolutions. This technique uses a hierarchical system of grids, meaning that a finer grid is placed over the coarser grid in the required areas, as can be seen in Figure 2.4. The refinement process can be repeated recursively from coarser ones until no refinement is needed or the finest refinement level is reached. An optimal time-stepping for each grid is achieved with refinement of the sub-grids in both time and space, thus resulting in reduced truncation error. Interpolation and flux correction at grid edges allow for conservation laws to be maintained and a synchronization between grids at different levels to be achieved. Each sub-grid at different refinement level in the hierarchy is uniform and its solution can be advanced individually using the numerical integration scheme with time step adaptively modified by the same refinement factor as in space. More accurate solutions at finer level grids are projected back onto the coarser meshes when they both advanced to the same time step. In order to follow moving features of the flow, all adaptively refined sub-grids are regenerated after a specific number of time steps on the base grid level. The re-gridding procedure in the AMR algorithm therefore dynamically creates, moves and

destroys sub-grids in the hierarchy so that refined regions occur only where they are needed as the computation progresses.

The domain areas requiring refinement are identified by an indicator function, which measures the total error produced locally by the simulation at the coarser grid. In compressible flows, an estimator of this error is the numerical density gradient. Cells are flagged for refinement if:

$$\sqrt{\left(\frac{\rho_{i+1,j}-\rho_{i-1,j}}{x_{i+1}-x_{i-1}}\right)^2+\left(\frac{\rho_{i,j+1}-\rho_{i,j-1}}{y_{j+1}-y_{j-1}}\right)^2} > \varepsilon_{ref}$$

where ε_{ref} is the reference error. Reducing the reference error leads to more areas of the domain requiring refinement, therefore the computational time increases.

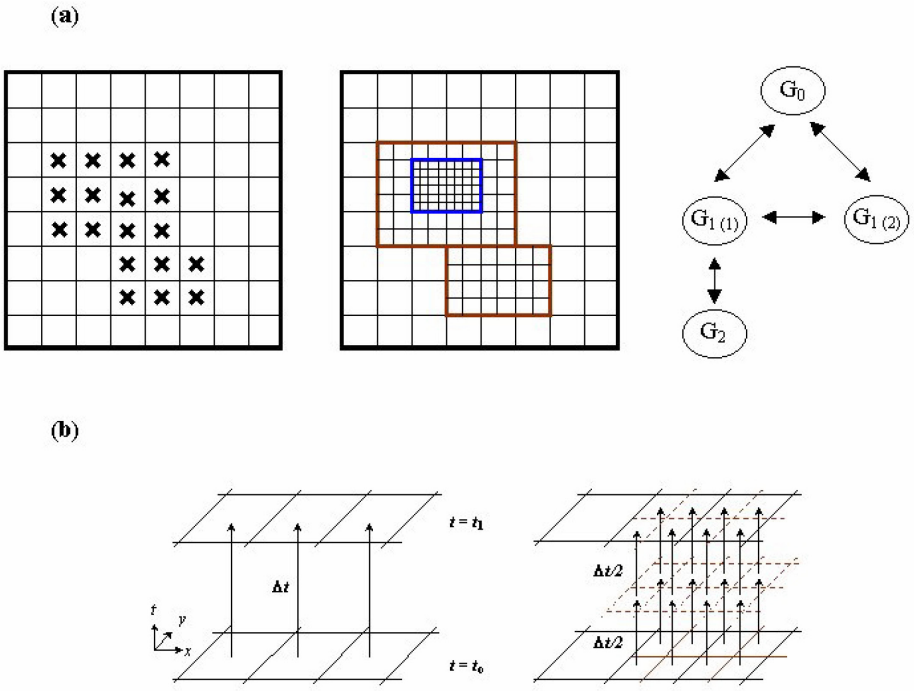

Figure 2.4 *Hierarchical series of Cartesian grids for adaptive refinement in two-dimensional configuration. (Ng 2005)*

Further technical details of the AMR algorithm applying to general hyperbolic systems of conservation laws can be found in articles by Berger & co-workers (Berger & Oliger 1984; Berger & Colella 1989; Berger & LeVeque 1998; etc.) and are not discussed in any depth here. In the present study, the TVD-WAF method has been implemented in an existing framework AMR C++ code originally developed by Hern (1999) and improved by Bates (2005).

2.4 Computational time step

In this study, the CFL (Courant, Friedrichs, Lewy) number is chosen before beginning the simulations with a value equal to 0.9. As discussed early, the time step is computed based on CFL number for each time step from the equation:

$$\Delta t = C_{cfl} \frac{\Delta x}{S_{max}^{(n)}}$$

where Δx is the mesh spacing & $S_{max}^{(n)}$ the maximum wave speed present at time level n, given by equation:

$$S_{max}^{(n)} = \max_i \{|u_i^n| + a_i^n\}$$

2.5 Numerical scheme validation

2.5.1. Sod's shock tube problem

The standard benchmark test to assess the accuracy of the WAF method in solving the Riemann problem is the canonical Sod's problem. This is a shock tube, closed at the two ends and it initially has a diaphragm, located at 0.3, separating two distinct areas with specific initial conditions (pressure, velocity and density). The initial conditions considered for this problem are $(\rho_L, u_L, P_L) = (1, 0, 1)$ and $(\rho_R, u_R, P_R) = (0.1, 0, 0.1)$. At t = 0 the diaphragm is removed, and the resulting flow is computed using the WAF method, along with an approximate HLLC Riemann solver and a van Leer limiter. The CFL number was chosen equal to 0.9, γ = 1.4 and 100 cells for the domain. The solution of this problem after t = 0.2 s and 56 time-steps can be seen in Figure 2.4.

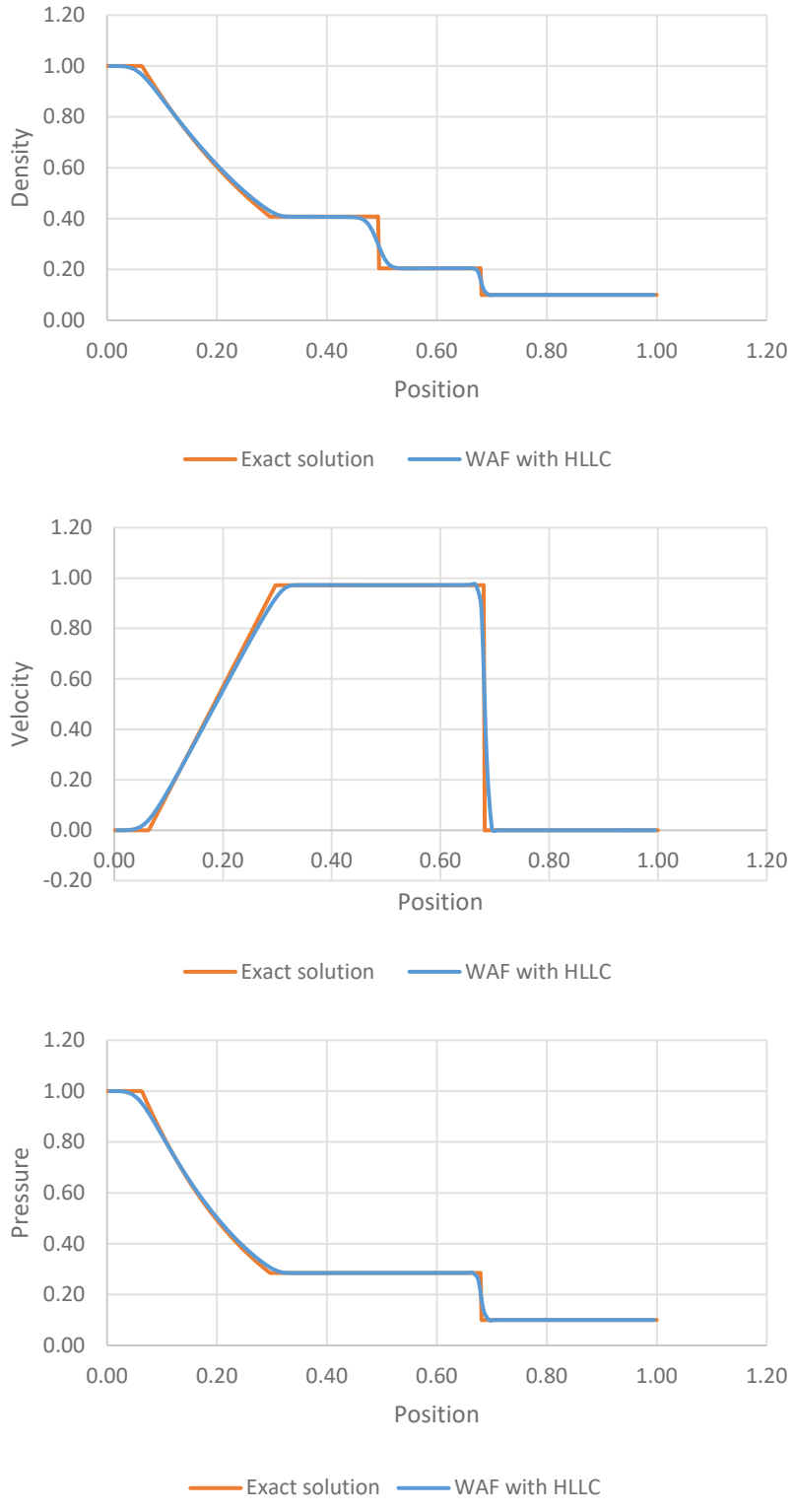

Figure 2.5 *Density, velocity and pressure plots for exact and approximate solution of Sod's shock tube problem*

From the above figures the presence of a right shock wave, a contact discontinuity and a left sonic rarefaction wave can be seen. The solution has high accuracy and because of the Van Leer limiter, there are no spurious oscillations. The right shock wave, located at ≈0.7, can be identified since $p^* > p_R$. It is compressive in nature and it results in very rapid changes of physical quantities. The central contact discontinuity is located at ≈0.5. Pressure and velocity remain the same, whereas density changes. Finally, the left rarefaction wave is located between ≈0.3 (fan tail) and ≈0.1 (fan head). It can be identified by $p^* \leq p_L$ and there is a smooth transition of pressure, velocity and density.

2.5.2. One-dimensional pulsating detonation

Instabilities associated with the one-dimensional planar ZND structure have been revealed by Erpenbeck (1962, 1964) via a linear stability analysis. The non-linear intrinsic oscillatory behavior of one-dimensional detonations with simple chemistry has also been shown numerically by Fickett & Wood (1966) using the method of characteristics. Since then, more thorough studies on one-dimensional pulsating detonations have been carried out by numerous researchers (see, for example, Bourlioux et al. 1991; He & Lee 1995; Sharpe & Falle 1999; etc.) and this canonical 1-D unsteady detonation problem has become a widely used benchmark problem for assessing high-resolution numerical schemes for detonation simulations. Therefore, this problem is used to evaluate the performance of the described TVD-WAF method together with the operator splitting in the context of detonation simulation.

The computational setup follows Bourlioux et al. (1991) by fixing the dimensionless parameters with the values $Q/RT = 50$; $\gamma = 1.2$; $E_a/RT = 50$ and overdriven factor $f = 1.6$ (i.e., $f = (D/D_{cj})^2$ where D is the overdriven detonation velocity and D_{cj} is the minimum Chapman-Jouguet detonation velocity which can be obtained analytically using the thermodynamic equilibrium calculation. These parameter choices, according to a number of linear stability analyses, give a single instability mode. Various numerical computations also show that the nonlinear manifestation of this instability is a regular periodic pulsating detonation (Bourlioux et al.1991; He & Lee 1995; etc.). A grid resolution of 20 points per $L_{1/2}$ (the characteristic reaction length behind the shock where half of the reactants are being consumed) is used. This resolution is usually required for reasonably accurate resolution of the detonation wave with an overdrive of

f = 1.6 if an upwind numerical scheme is used as found by Hwang et al. (2000). The sub-plot in Figure 2.6 shows the leading shock pressure versus position plot generated using the WAF scheme. After the transient development due to the initial conditions used, it correctly predicts the single instability mode of the detonation front. From the same plot, one can look at the peak pressure magnitude reached during the limit-cycle pulsations. The present result agrees closely with the peak pressure value of ~98.6 as first predicted by Fickett & Wood (1966) and those obtained from other various numerical schemes (Hwang et al. 2000).

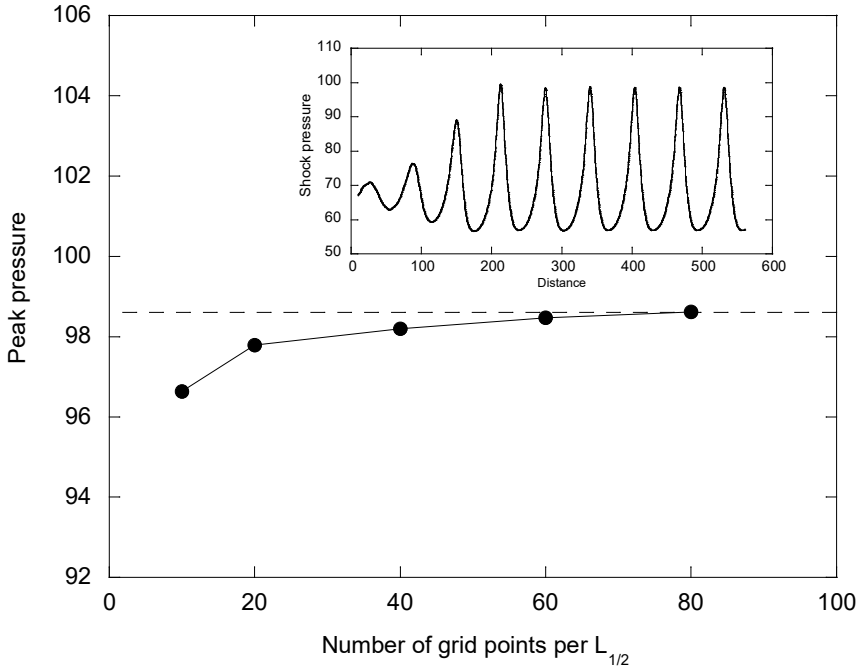

Figure 2.6 *Resolution study of one-dimensional pulsating detonation*

2.6 Summary

In this chapter, the mathematical model governing the reactive flow dynamics of shock-multiple flames interaction is presented. The applicability of a high-order upwind scheme, namely the WAF scheme, to solve numerically the governing equations for the simulation is also presented. The numerical scheme is also incorporated with adaptive mesh refinement. The Berger & Oliger's adaptive refinement technique improves the efficiency of numerical simulations of systems of partial differential equations by allowing the size of time steps and grids to vary adaptively according to the requirement of the evolving solution. Computational resources are not wasted in maintaining uninteresting parts of the solution at unnecessarily high resolutions. The numerical code is verified by applying to two canonical problems of compressible flows, namely the Sod's shock tube and one-dimensional pulsating detonation problem.

Chapter 3

Simulation Results of Shock-Multiple Flames Interaction

3.1 Introduction

The motivation of this thesis is focused on the question: *Can DDT be induced by shock multiple-flame interaction?* In this chapter, a series of computational simulations was performed to study the interaction of a planar shock with multiple cylindrical flame kernels, with the purpose of determining whether these interactions can cause a transition from deflagration to detonation (DDT). The essential flow features of the deflagration-to-detonation transition (DDT) resulted from such interaction between a weak shock with multiple laminar flame kernels are revealed and discussed.

3.2 Computational setup

The present simulation is carried out in two-dimensional configuration to look at shock-multiple cylindrical flame interactions. The governing equations, i.e., the reactive Navier-Stokes equations with a single-step Arrhenius chemistry, that describe the system and the numerical method used to approximate numerically the solutions, i.e., HLLC-TVD WAF with Strang's fractional operating splitting, are well detailed in Chapter 2.

Different material and chemistry properties of the reactive mixture are chosen to model a stoichiometric acetylene-air mixture and are detailed in Table 3.1. The majority of these values are adapted from Khokhlov et al. (1999), only with the transport properties and pre-exponential rate factor updated to match better the laminar flame speed and thickness (Bates 2005).

Mixture parameters	Value
Initial pressure p_o	1.33 x 10^4 Pa
Initial temperature T_o	293 K
Initial density ρ_o	1.58 x 10^{-1} kg/m^3
Flame temperature T_f	2340 K
Specific heat ratio γ	1.25
Molecular weight M	29
Chemical heat release Q	35.0 RT_o/M
Activation energy E_a	29.3 RT_o
Pre-exponential constant A	5 x 10^8 m^3/kg-s
Constant exponent n	0.7
Transport constants ν_o, D_o and α_o	2.4 x 10^{-7}

Table 3.1 *Initial condition and mixture model parameters (adapted from Khokhlov et al. 1999 and Bates 2005)*

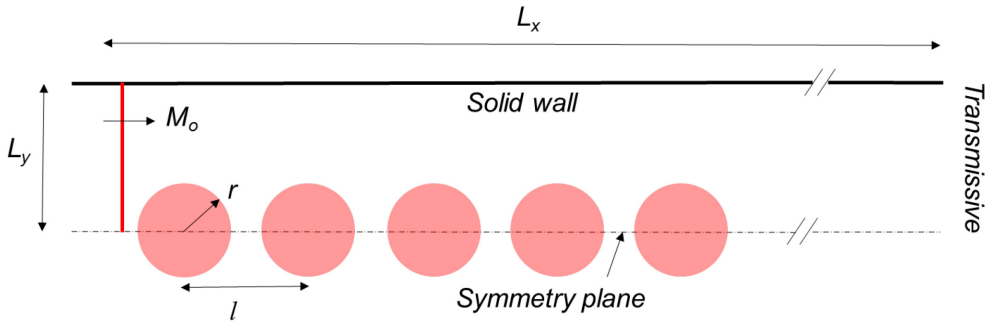

Figure 3.1 *Schematic of the computational setup for the two-dimensional simulation*

The schematic of the computational setup for the two-dimensional simulations is again shown in Figure 3.1 with a computational domain denoted by $L_x \times L_y$, an initial flame radius r, incident shock Mach number M_o, and distance between discrete flames l. The circles shown in Figure 3.1 represent initial flame kernels ignited before the shock passage. These are embedded in the

computational domain to approximate a sequence of low energy ignitions. For simplicity, these are set up as a discontinuity between cold reactants and hot products at constant pressure and adiabatic flame temperature T_f. The simulation is restricted to half of the domain, with a symmetry plane or reflective boundary condition applied along the lower boundary to minimize the computational expense. The top boundary is a non-slip solid wall for the Navier-Stokes computation. The left and right boundaries are transmissive. Unless specified otherwise, five levels of AMR grid refinement are used (2, 2, 2, 2, 2). The base resolution combined with AMR gives an effective resolution with Δx in the highest level equal to 47 μm.

Initially 12 flame kernels were considered in a computational domain with height L_y = 16.5 mm and total length L_x = 0.36 m. The choice is similar to the number of lateral ports for electrical igniters used experimentally in Frolov et al. (2003). The kernels were evenly spaced, separated by a distance l = 18 mm from each other (center to center). The initial radius of the kernels, referred to as flame amplitude, was set equal to r = 4.5 mm. The first kernel is located at a distance l_2 = 9 mm from the left boundary. A weak planar shock which has a velocity M_o = 1.8 is placed upstream of the first kernel, at a distance l_1 = 6 mm from the left boundary. Downstream of the shock wave the flow speed is set everywhere as zero, whereas upstream of the shock the flow properties are determined by the Rankine-Hugoniot condition.

3.3 Initial interactions

The driven shock reaches and interacts successively with the flame kernels as can be seen in Figure 3.2 and Figure 3.3. The pressure and the Schlieren-type density gradient plots from the Navier-Stokes simulations are first present in Figure 3.2. The Schlieren plots are used to provide visual identification of shocks, contacts and rarefaction waves within the flow and can be modelled numerically using the formula:

$$\varphi = exp\left\{-\epsilon \frac{|\nabla\rho|}{\max(|\nabla\rho|)}\right\}$$

where ϵ is an amplification factor for small gradients ranging from 20 to 100.

These figures first show the early evolution of the incident weak shock after interaction with the first few discrete flames. The interaction with the first flame kernel leads to the deformation of the kernel. Unburned cold material enters the hot burned region of the bubble and creates a funnel, as a result of the Richtmeyer-Meshkov (R-M) instability, occurring due to the acceleration of two fluids with different densities. This deformation leads to an initially reduced flame surface, which along with a reduced flame thickness, cause a reduction of the energy release rate. After the initial reduction, the flame surface starts to gradually increase, along with the energy release rate. The negative vorticity at the edges of the flame bubble, which has an increased strength at the upper edge due to higher angle of interaction with the shock, as can be seen in Figure 3.3, contributes to the flame surface increase by aiding the expansion of the flame vertically, and therefore the subsequent rise of the energy release rate.

The Schlieren plots of Figure 3.2 show that after the incident shock reaches the flame kernel, the top part continues to propagate downstream outside the kernel, whereas the bottom part of the shock is partially diffracted inside the kernel and partially reflected as a circular wave. A portion of this circular wave moves upstream as a rarefaction wave and the rest, after it reflects at the top boundary, either travels perpendicular to the initial shock or joins and amplifies the leading shock wave. Inside the flame kernel, the shock travels at a higher speed compared to the top part, and after multiple reflections and diffractions, a shock emerges from the right side of the bubble, followed by subsequent faster waves that join the leading wave and further amplify its strength. This is evident by the pressure increase behind the leading shock at later times in the pressure plots

of Figure 3.2. Similar shock reflections and diffractions repeat for the all the subsequent kernels as they interact with the shock waves.

Other noticeable features are that the other laminar, cylindrical flames in front of the shock are seen to have maintained their circular shape as they continue to burn outwards. Additionally, it is clear that a single weak shock–flame interaction was not enough to prompt DDT as concluded in Khokhlov et al. (1999).

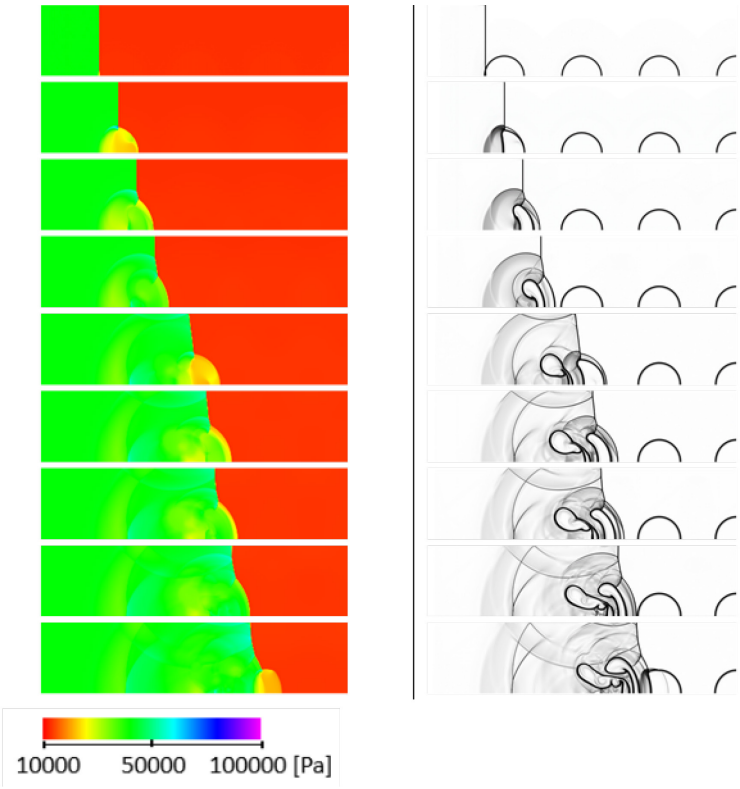

Figure 3.2: *Pressure and Schlieren plots, early shock-flame interactions*

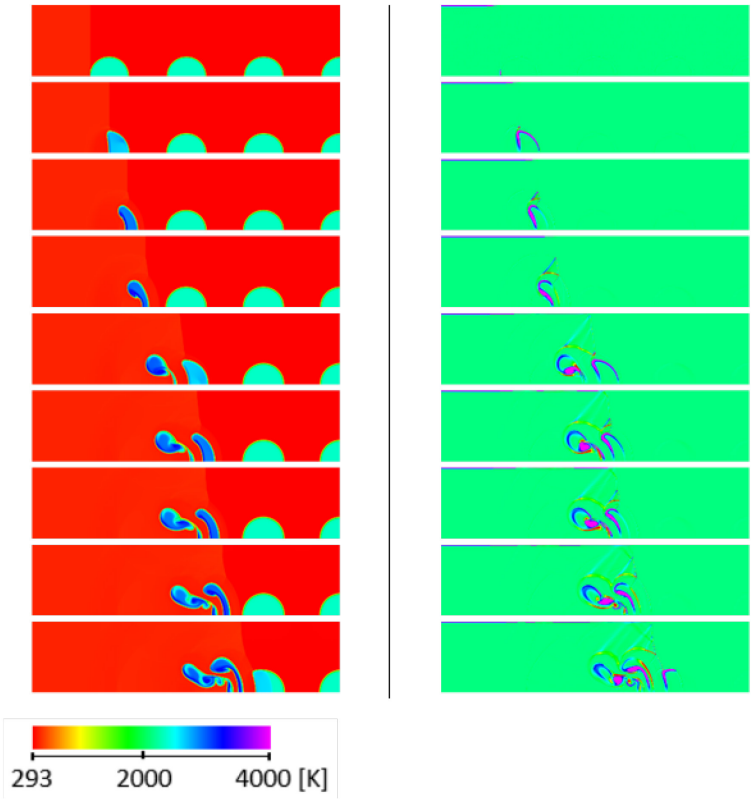

Figure 3.3: *Temperature and vorticity plots, early shock-flame interactions*

3.4 Multiple shock-flame interactions

The shock wave proceeds to interact with the rest of the flame kernels, resulting to intense mixing, turbulence and coalescence of flames to form a larger flame brush. The flame surface gradually increases, and along with an increased generation of turbulence they lead to a higher energy release rate. This in turn leads to an increase of flame speed and the transformation of the laminar flame brush to turbulent. In order for a successful DDT to occur, the flame brush has to continue accelerating, until achieving a critical deflagration speed, which corresponds to a sudden change to the mode of chemical reaction propagation. This deflagration velocity is of the order of half the CJ detonation speed V_{CJ}. The deflagration is able to propagate at this supersonic speed, relative to fixed laboratory coordinates, due to the precursor shock ahead of it. This means that the reactants ahead of the flame are not at rest, and therefore the propagation speed of the reaction font relative to the reactants is subsonic, in accordance to the subsonic nature of a deflagration wave.

The dominant mechanisms involved in the acceleration of the flame brush are different for low and high flame speeds. In low speeds, flame stretching and folding due to thermal expansion and fluid instabilities distort and increase the flame surface, leading to an increase of the energy release rate. In higher speeds, flame acceleration is mainly due to the burn out rate of flame folds, caused by the increased presence of small-scale turbulence which can be seen in the last panel of Figure 3.4. The interaction with the boundary layer also contributes to the flow acceleration. The boundary layer contains a velocity gradient that leads to the bifurcation of the shock wave, thus creating a recirculation zone which accelerates the flow.

The flow ahead of the flame brush is affected by compression waves that have been generated by the deflagration process and propagate downstream. These waves increase the temperature of the reactants, leading to increased reaction rate. However, temperature increase plays only a minor role in the phenomenon. Although it leads to higher flame velocity, it also leads to higher Mach number and therefore higher flame speed is required to generate shock waves. Increased temperature also results in reduced density of unreacted mixture, and therefore reduced energy release rate. The compression waves ahead of the flame brush also affect the flame kernels, and as a result they move downstream and slightly deform, becoming less circular on their left side. It

should be noted also that until the flame kernels interact with the incident shock, they continue to burn outwards due to heat and mass diffusion and increase in size.

In the temperature fields of Figure 3.5, the flame brush development after multiple interactions is shown. Between the flame kernels and the top boundary an induction zone of initially increased size exists, however it gradually reduces in size due to the elongation of the flame brush in the y direction.

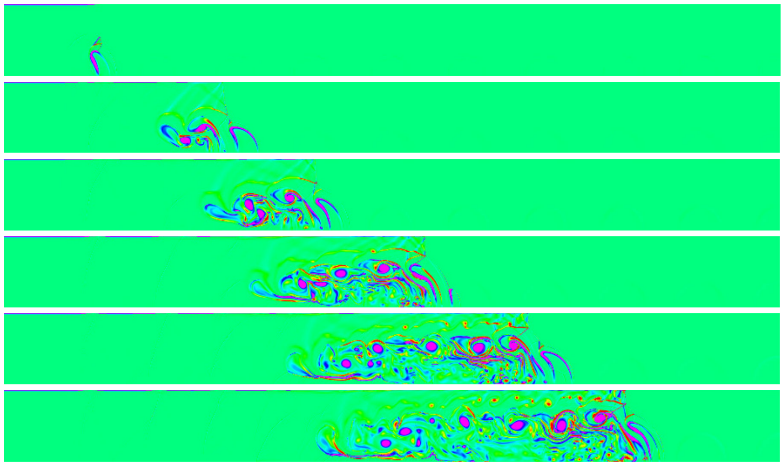

Figure 3.4: *Vorticity development after multiple interactions*

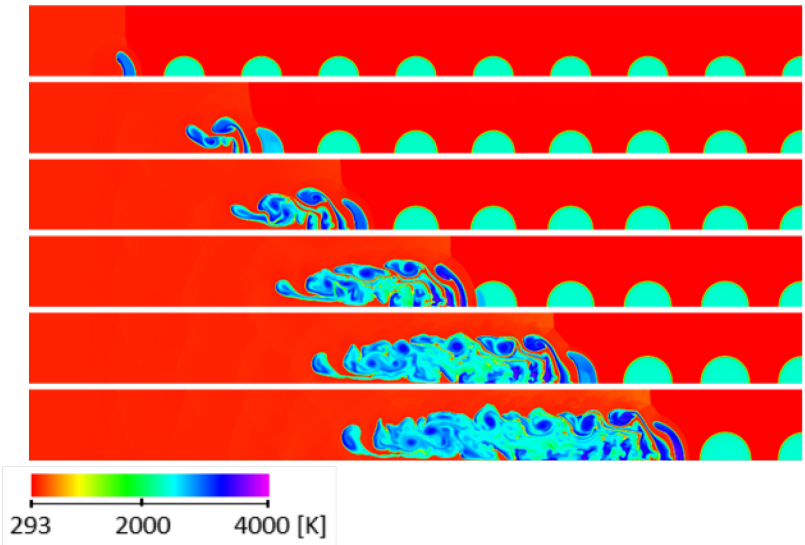

Figure 3.5: *Temperature development after multiple interactions*

3.5 Onset of detonation

Following the acceleration of the flame brush to a critical deflagration speed, the second requirement of the DDT process has to be met: The creation of proper local conditions, so that an explosion can occur, followed by proper amplification which will lead to the formation of a detonation wave. The amplification mechanism is known as Shock Wave Amplification by Coherent Energy Release (SWACER). This mechanism relies on the chemical energy being released in coherence with the generated shock wave, therefore strengthening the shock as it propagates.

In Figure 3.6 the onset of detonation for this simulation can be seen. Unreacted material is constrained between two highly turbulent flame brushes. A blast wave is generated at the point of minimum induction time and directed outwards, towards the gradient of reactivity. This spherical wave is a combination of a detonation, a retonation and a transverse wave. The transverse wave reflects at the top and bottom boundaries and the retonation wave propagates upstream in the combustion products. The detonation wave continues to amplify and propagate downstream in the preconditioned mixture behind the leading shock wave, until it fully develops to a multi-headed detonation wave. It should be noted that the detonation formed at this hot spot is initially highly overdriven, similarly to the direct initiation of a spherical detonation.

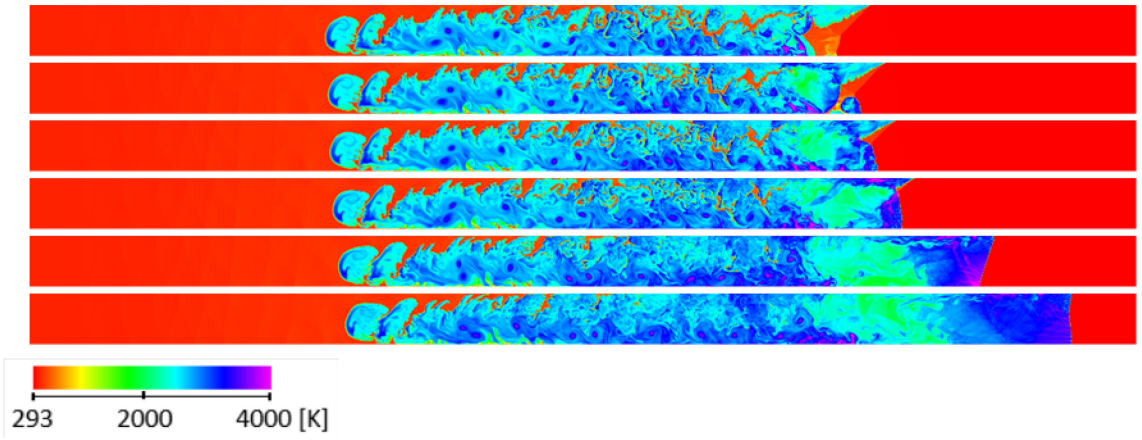

Figure 3.6: *Temperature plots, onset of detonation*

In Figure 3.7, Schlieren plots focused at the location where the onset of detonation occurs are presented. The retonation wave travelling upstream can be seen in the second image. Also it can be seen that the initial spherical blast wave is followed by multiple reflections and diffrations at the boundaries and the flame brush. In the last panel, the frontal cellular structure of the fully developed multiheaded detonation wave is shown.

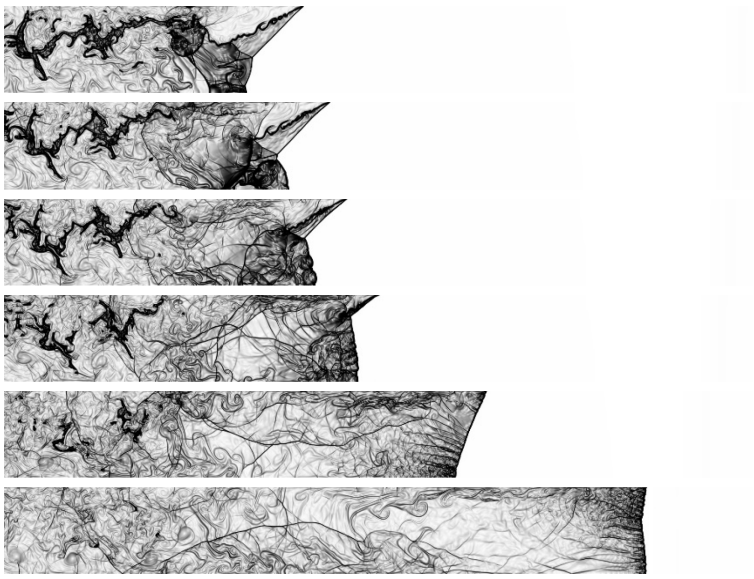

Figure 3.7: *Schlieren plots focused at the onset of detonation*

3.6 Resolution study

In order to verify whether the grid resolution is adequate and does not significantly affect the results, one more simulation was performed with increased grid resolution. An additional AMR level was added, leading to a resolution of Δx = 23.5 μm at the highest level. The results can be seen in the temperature plots of Figure 3.8. In general, the flow development is similar to the original resolution simulation, with close run-up distance and onset time. In both cases onset of detonation occurs in unreacted material that is confined between turbulent flame brushes. Due to the higher resolution, finer details of the flow appear, and the flame brush surface appears to be more wrinkled compared to the normal resolution simulations. These additional small wrinkles mean that an increased flame surface is present, which leads to a higher energy release, and thus a faster acceleration of the flame brush. This explains the slightly earlier position of the hot spot in this simulation. Therefore, as demonstrated, the original grid resolution of Δx = 47 μm is sufficient for the simulation of the phenomenon.

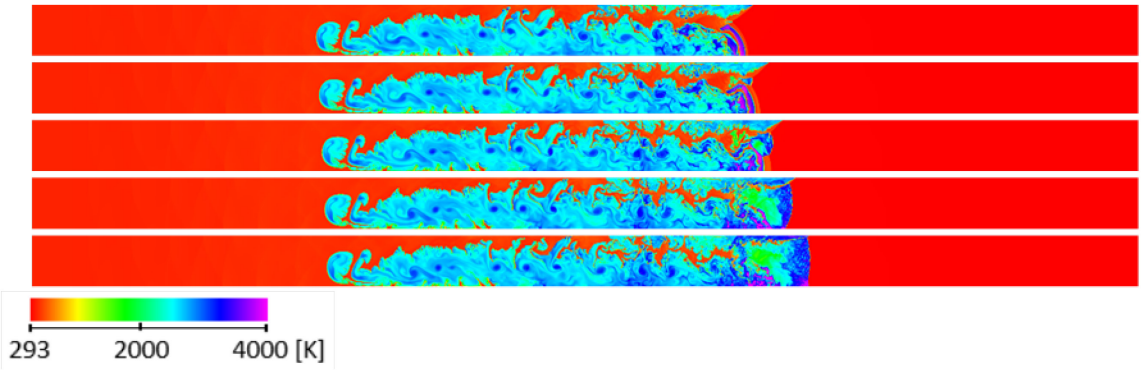

Figure 3.8: *Temperature plots, onset of detonation for Navier-Stokes simulation with double resolution*

3.7 Physical diffusion and viscous effects

A simulation with the effects of viscosity, thermal conduction and molecular diffusion removed from the governing equations is performed to determine their impact on DDT. The results of the simulation can be seen in Figure 3.9. Multiple wave reflections between the bottom boundary and the flame brush surface lead to the conditioning of the fuel-air mixture and the onset occurs at the reflective boundary. The transition to a detonation wave does not occur inside the domain boundaries. However, based on the onset of detonation that occurs at the symmetry boundary near the end of the domain, the detonation wave will likely form outside the domain boundaries. Compared to the simulation with Navier-Stokes equations, the onset of detonation occurs further downstream and at significantly later time. These results therefore indicate that the suppression of turbulence and of the burning rate strongly affects the DDT phenomenon.

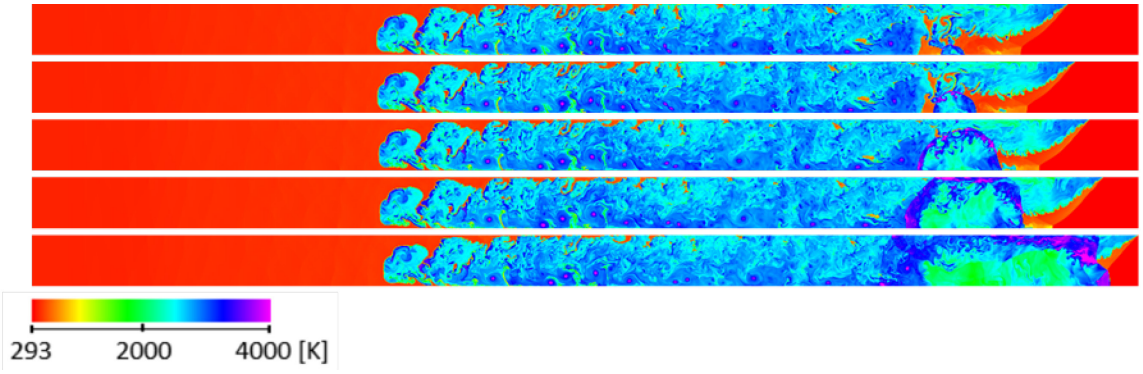

Figure 3.9: *Temperature plots, onset of detonation for Euler equations*

3.8 Summary

The present resolved, two-dimensional numerical simulations have been obtained to observe the propagation of a weak incident shock wave into multiple cylindrical flames and its subsequent amplification via intense wave interactions and reflection. The simulation results demonstrate that DDT is possible via a series of shock-flame interactions. In the Navier-Stokes simulation, the onset of detonation is observed from the development of a hot spot ahead of the flame brush through an increase in the energy release caused by the increase of flame surface area and the higher shock temperatures from amplifying shock near the top wall through pressure wave reflection and coalescence. In the absence of physical diffusion and viscosity where turbulence and the burning of the turbulent flame brush is suppressed, the Euler simulation also show that the intense flow fluctuations generated by the interactions of shocks, boundary and flames can still create the conditions under which deflagration-to-detonation can be realized.

Chapter 4

Parametric Study

4.1 Introduction

DDT in a smooth tube is a stochastic and sensitive phenomenon which can vary significantly even under a small parameter change, leading to different characteristics (run-up distance and onset time), whereas the transition might not even occur inside the domain boundaries, as was demonstrated previously for the simulation with Euler equations. For that reason, a series of numerical simulations were performed in which certain parameters were modified to determine their impact on DDT and identify the changes that could lead to a reduction of the run-up distance and time the onset of detonation occurs.

4.2 Channel height

The first simulation parameter under consideration was the domain height. The values that were considered were between 12 mm and 16.5 mm, since that was the highest value for which DDT would occur inside the domain and was not affected by the domain resolution, as was demonstrated in Chapter 3. The choice of reducing the domain height was made in order to increase the effect of shock-boundary layer interaction in the transition process and was indicated by the increased size of the induction zone near top boundary at the original simulation. The results of the simulations can be seen in Figure 4.1 & Figure 4.2.

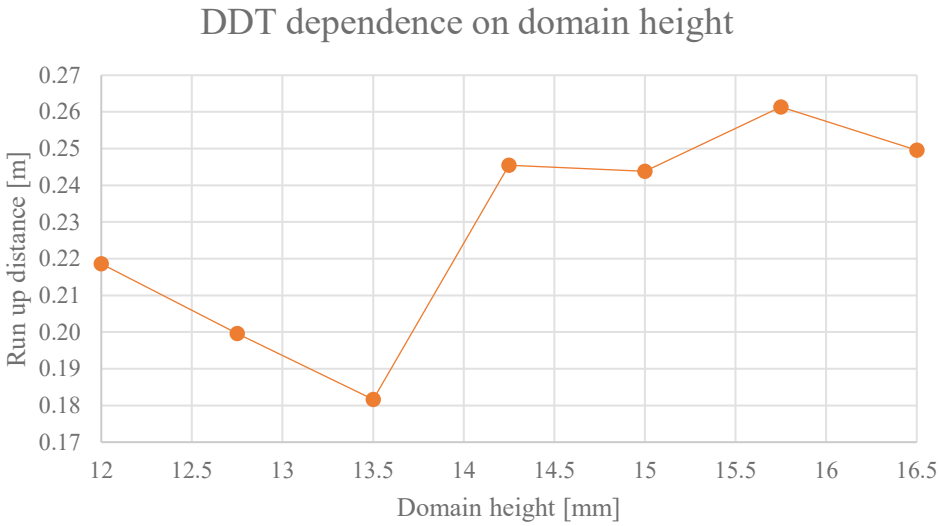

Figure 4.1: *Run up distance dependence on domain height variation*

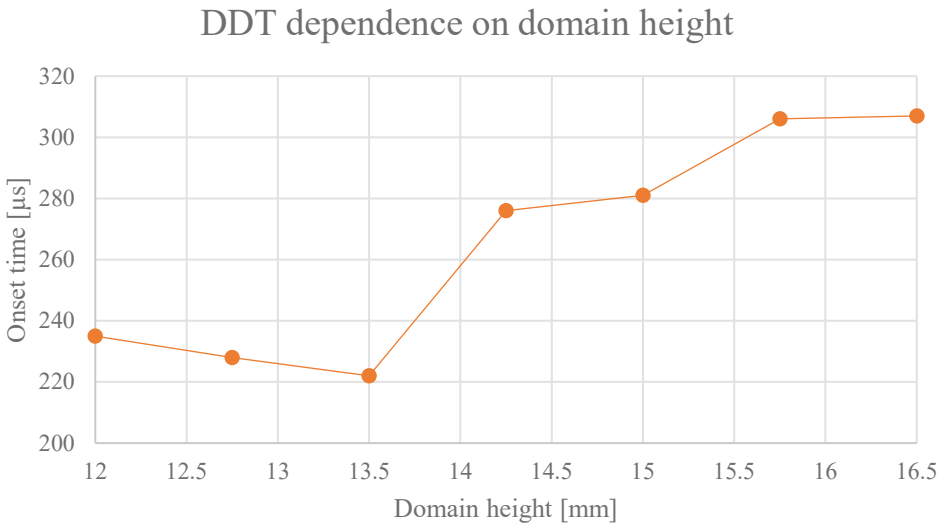

Figure 4.2: *Onset time dependence on domain height variation*

As can be seen in these figures, reducing the domain height from the initial value of 16.5 mm leads to the reduction of characteristic values of DDT, up to a minimum for the simulation with 13.5 mm domain height. For that simulation, the run up distance is equal to 0.18 m and the onset

time equal to 222 μs. Further reduction of the domain height leads to a significant increase of run up distance, whereas onset time varies only slightly.

Figure 4.3 shows the temperature plots at the onset of detonation for three simulations with 13.5 mm, 14.25 mm and 16.5 mm domain heights. For the simulation with the minimum run up distance, the onset of detonation occurs above 10th flame kernel, where a local explosion is induced near the top solid boundary due to viscosity and wave reflections. The minimal run up distance observed is a result of the increased contribution of the shock-boundary interaction in the transition process as well as the proper synchronization of the chemical energy release with the shock wave. Reducing the channel height promotes compression wave reflections and the role of turbulence induced by the boundary layer becomes more significant.

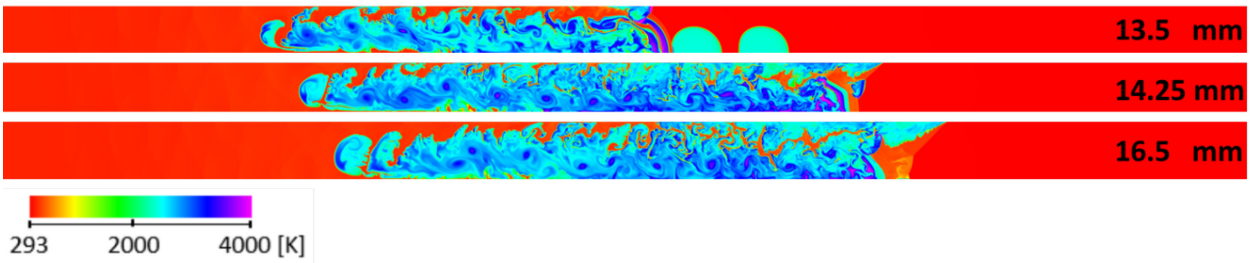

Figure 4.3: *Temperature plots at the onset of detonation for 13.5 mm, 14.25 mm and 16.5 mm domain height*

4.3 Flame amplitude

The second parameter to be modified was the amplitude of the flame kernels. Practically, this parameter can be controlled by different spark ignition times in real experiment. For this series of simulations, the domain height was considered equal to 15 mm, 5 levels of AMR were used with the same resolution at the top level as previously. The amplitude values considered were between 4.4 mm and 6.6 mm. The results from these simulations can be seen in Figure 4.4 and Figure 4.5.

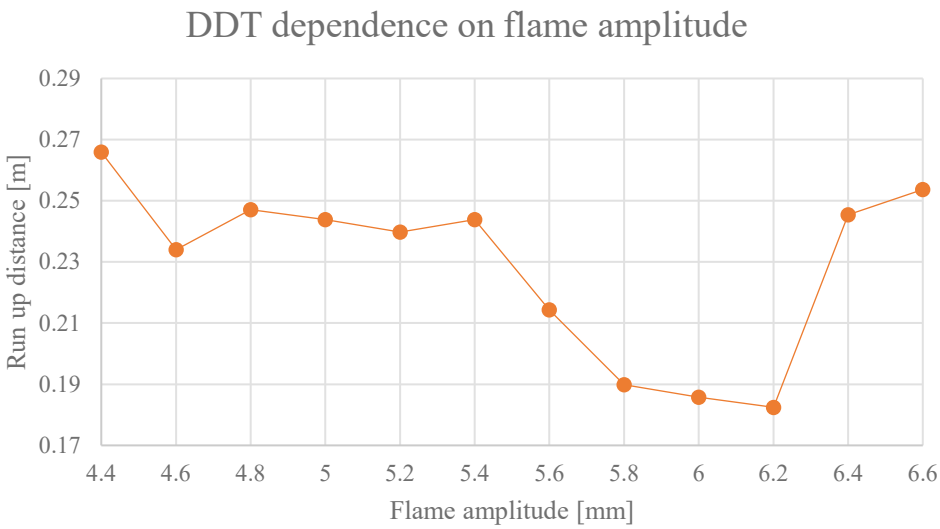

Figure 4.4: *Run up distance dependence on flame amplitude variation*

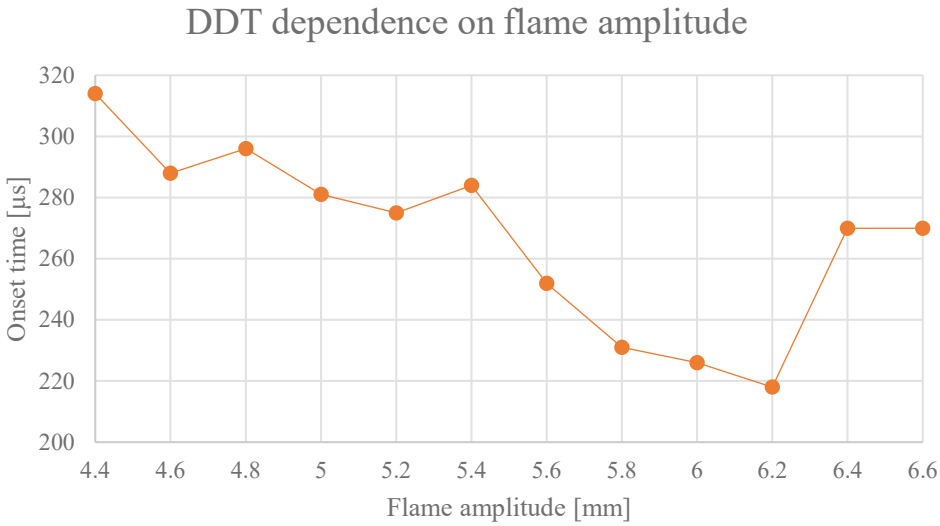

Figure 4.5: *Onset time dependence on flame amplitude variation*

Increasing flame amplitude has a positive impact on DDT. Larger flame amplitude implies larger flame surface; the RM instabilities from the shock-flame interaction will also become severe as the flame amplitude increases. As the amplitude is increased, the values of distance and time start to gradually reduce, until the flame amplitude of 5.4 mm. Then, there is a significant reduction when flame amplitude is increased from 5.4 mm to 5.8 mm, followed by a slight reduction until 6.2 mm and finally a significant increase for higher values. Similarly to the domain height variation, this time and run-up distance reduction up to 6.2 mm is due to the increased effect of shock-boundary layer interaction, whereas the increase in the end is due to the effect on the formation of the Mach stem, and therefore DDT can not occur as easily.

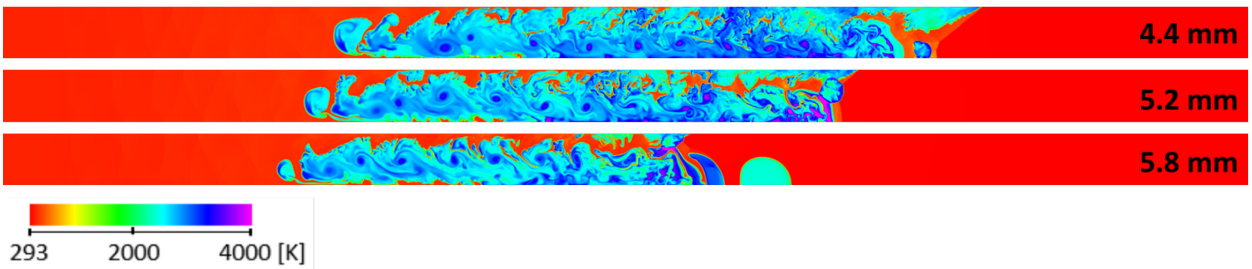

Figure 4.6: *Temperature plots at the onset of detonation for 4.4 mm, 5.2 mm and 5.8 mm flame amplitude*

4.4 Flame kernel spacing

In this series of simulations the distance between flame kernels was modified for a domain height equal to 15 mm, 5 AMR levels and the same resolution Δx = 47 μm at the highest level. Similarly to the flame amplitude, practical flame kernel spacing is achieved by using different spark distance and properly controlling the spark timing to generate each flame kernel. When the distance between flame kernels is shorter then there are more shock-flame interactions per unit length, which results in increased acceleration of the flame brush. On the contrary, Mach stems can form when the distance between the flame kernels is large enough and thus DDT is more likely to occur. The combination of these two effects leads to the results shown in Figure 4.7 and Figure 4.8.

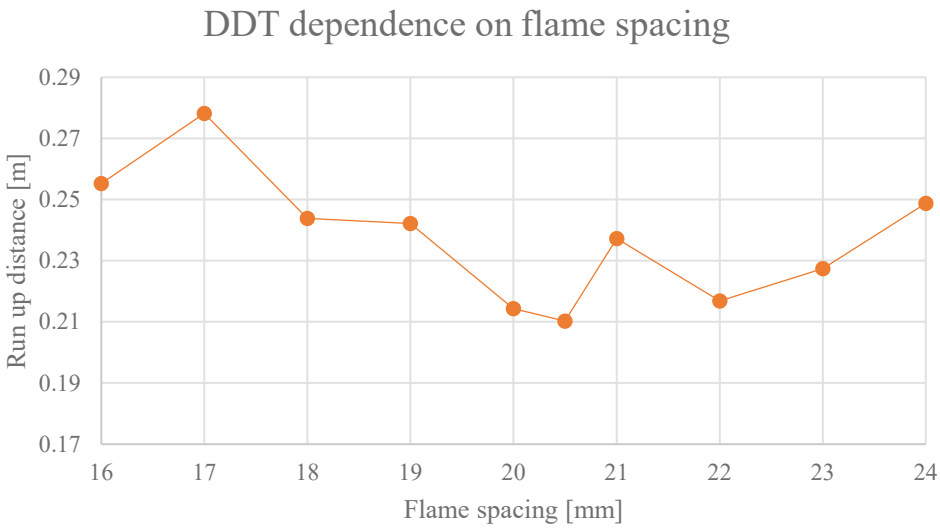

Figure 4.7: *Run up distance dependence on flame kernel spacing variation*

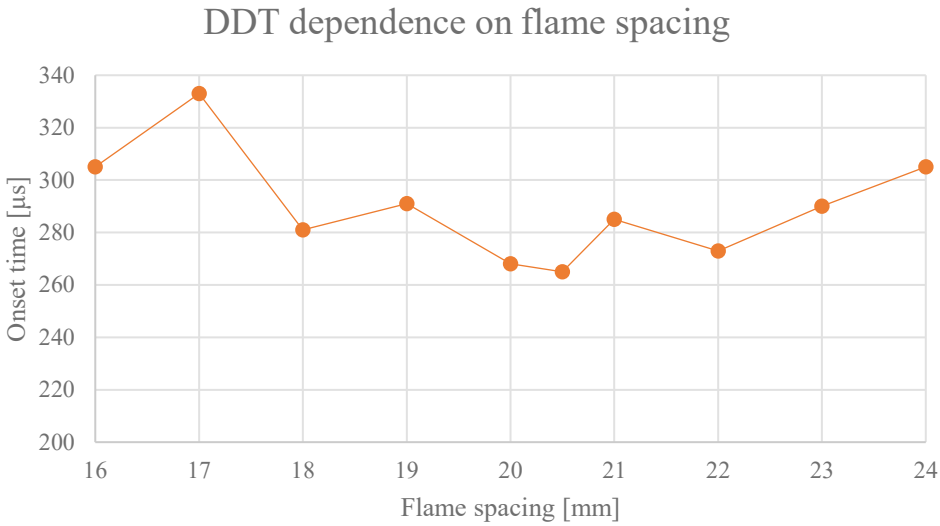

Figure 4.8: *Onset time dependence on flame kernel spacing variation*

The results show that increasing the flame spacing leads to a reduction of run up distance and time with minimum values for flame spacing 20.5 mm, followed by an increase for higher flame spacing values. In Figure 4.9 the temperature plots for 17 mm, 19 mm and 20.5 mm are shown. The minimum run-up distance corresponds to an onset of detonation near the top boundary. For the 17 mm case, which has the maximum run up distance, the onset of detonation is a result of the multiple wave reflections between the bottom reflective boundary and the flame brush and occurs almost simultaneously at two locations at the reflective boundary.

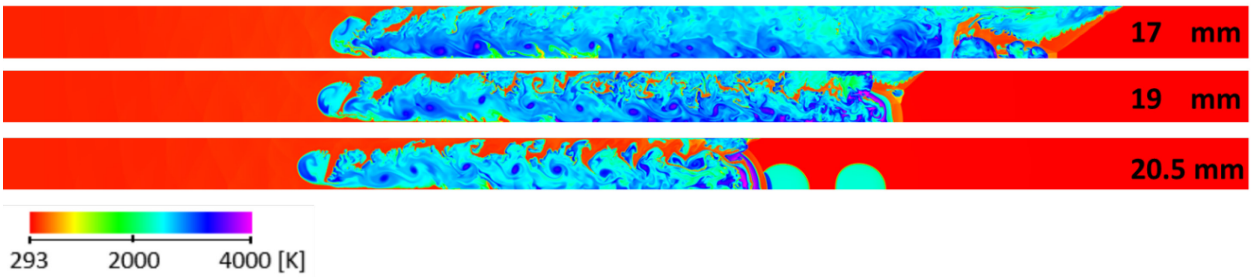

Figure 4.9: *Temperature plots at the onset of detonation for 17 mm, 19 mm and 20.5 mm flame kernel distance*

4.5 Shock wave position

As previously mentioned, the flame surface has been modeled as a contact discontinuity between the unburned cold reactants and hot combustion products. Having a discontinuity instead of a distribution could potentially affect the DDT phenomenon. For that reason, the incident shock wave was placed further upstream, while maintaining all other parameters same, in order to allow the flame kernels to create a distribution near the flame surface in the additional time until the first shock-flame interaction occurs. The shock placements considered were at 1 mm and 3 mm distance from the left boundary and the results were compared to the original 6 mm placement.

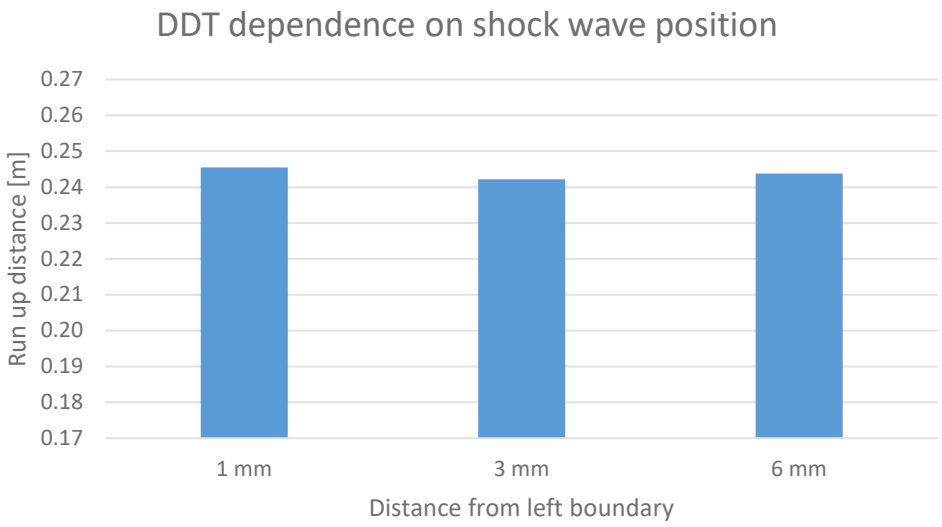

Figure 4.10 : *Run up distance dependence on shock wave position*

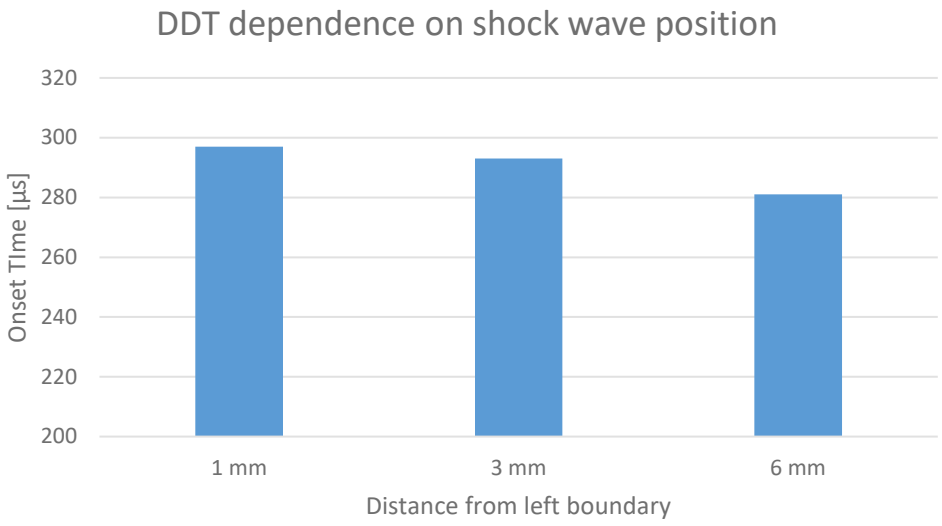

Figure 4.11: *Onset time dependence on shock wave position*

As can be seen in Figure 4.10 & Figure 4.11, shock wave placement has no significant effect and run up distance is essentially constant. The small onset time difference can be attributed to the additional required time until the shock begins interacting with the first flame kernel. Therefore, modeling the flame surface as a contact discontinuity compared to a distribution does not affect the phenomenon.

4.6 Incident shock strength

In this series of simulations the incident shock speed was reduced to a value of $M_o = 1.6$, while maintaining all other parameters constant. These simulations showed that this weaker incident shock can induce DDT and that the onset time was higher for all simulations. However, the effect on run-up distance was not clear, since there were numerical simulations with higher run-up distance and others with lower one. This demonstrated the need for further examination and for additional simulations to be performed. For that purpose, modifications of the domain height, flame spacing and the flame amplitude were performed for incident shock velocity $M_o = 1.6$, and the results were compared to the ones for the original $M_o = 1.8$ shock speed, as can be seen in figures 12- 17.

Looking at those figures, the simulations with $M_o = 1.6$ demonstrate similar behaviour, however they appear to be more sensitive, with larger variations of characteristics and the graphs appear shifted compared to the originals. This shifting can be attributed to the required proper synchronization of the chemical energy release with the propagating shock. The comparison of the lowest characteristic values for $M_o = 1.6$ and $M_o = 1.8$ shows that increasing the incident shock velocity accelerates DDT and moves the location of the hot spot further upstream. A stronger incident shock results in higher temperature of the shocked reactants, and therefore a lower induction time, meaning that smaller hot spots can auto-ignite.

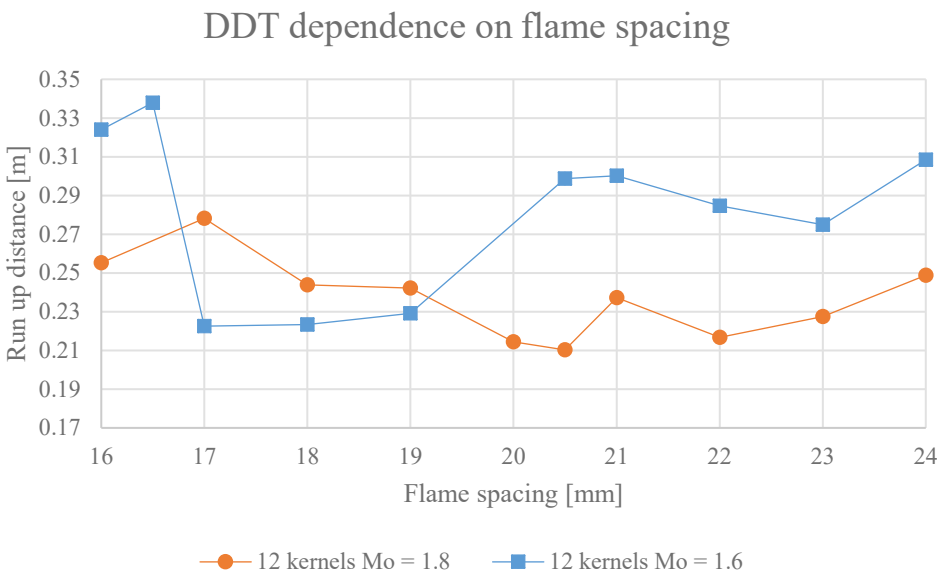

Figure 4.12: *Run up distance dependence on flame kernel spacing for incident shock velocities $M_o = 1.6$ and $M_o = 1.8$*

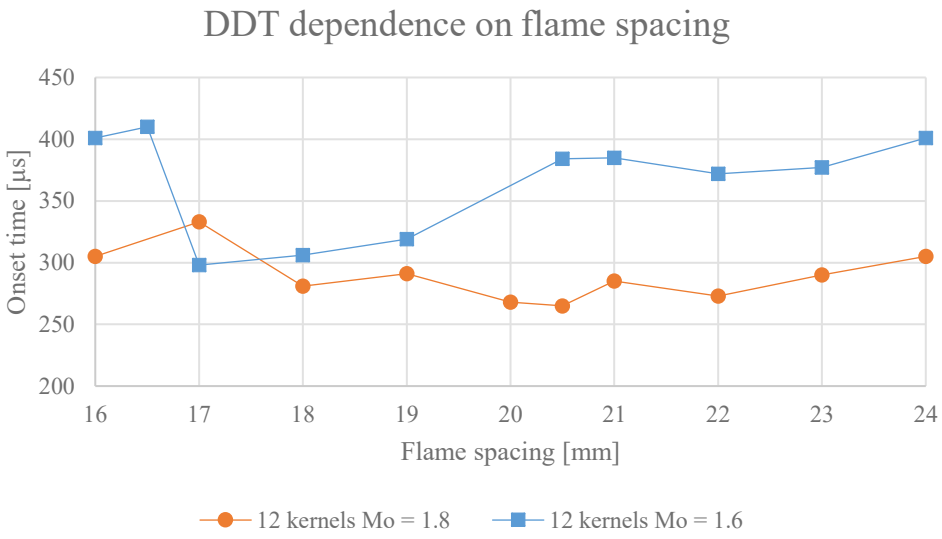

Figure 4.13: *Onset time dependence on flame kernel spacing for incident shock velocities $M_o = 1.6$ and $M_o = 1.8$*

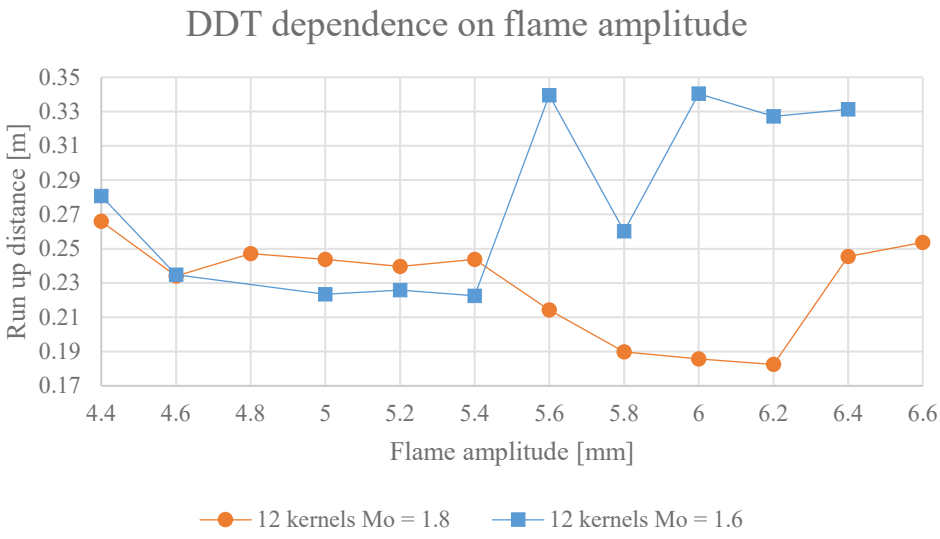

Figure 4.14: *Run up distance dependence on flame kernel amplitude for incident shock velocities* $M_o = 1.6$ *and* $M_o = 1.8$

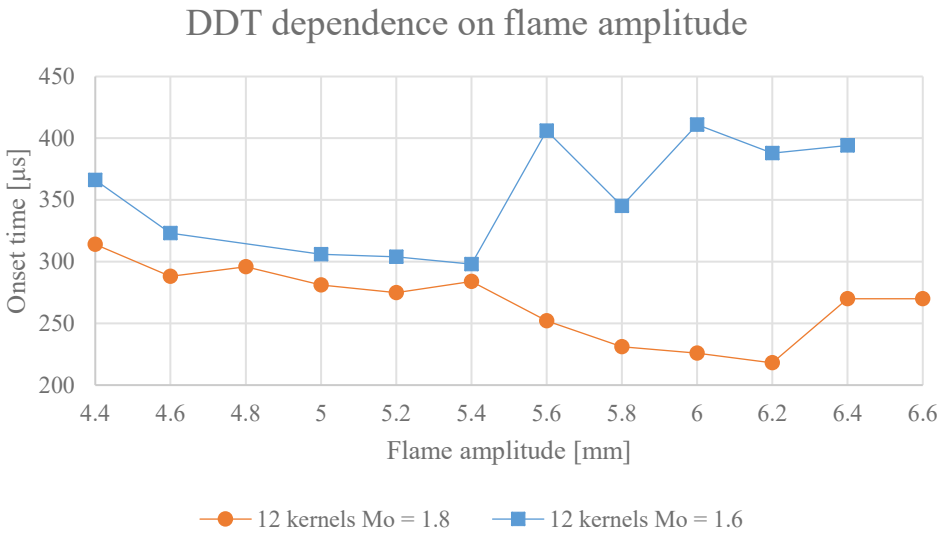

Figure 4.15: *Onset time dependence on flame kernel amplitude for incident shock velocities* $M_o = 1.6$ *and* $M_o = 1.8$

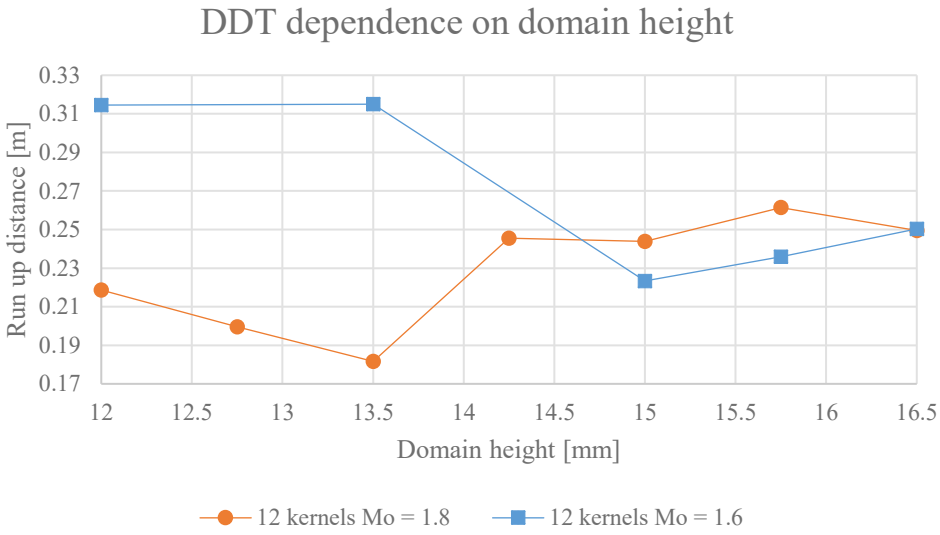

Figure 4.16: *Run up distance dependence on domain height for incident shock velocities* $M_o = 1.6$ *and* $M_o = 1.8$

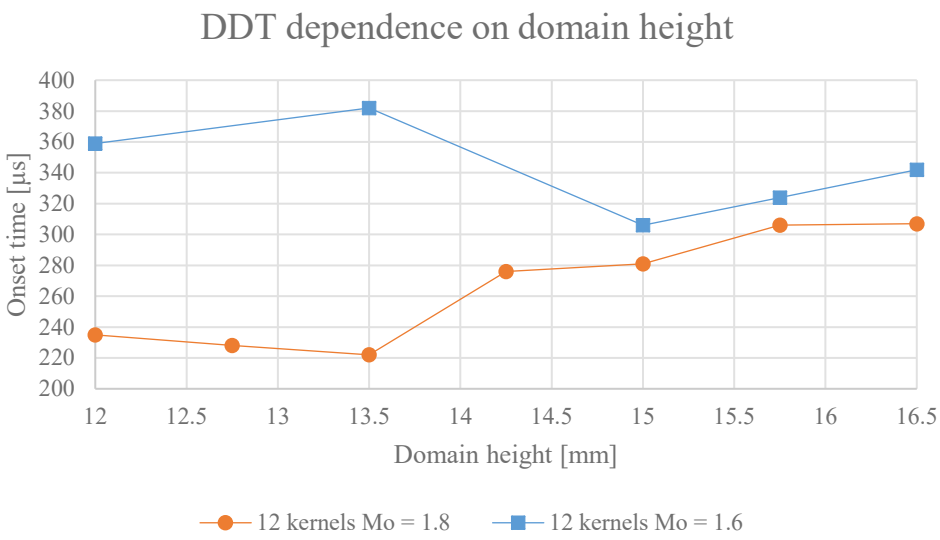

Figure 4.17: *Onset time dependence on domain height for incident shock velocities* $M_o = 1.6$ *and* $M_o = 1.8$

4.7 Number of flame kernels

Finally, the simulations with domain height, flame amplitude and spacing modifications were repeated for an incident shock wave interacting with 10 flame kernels instead of 12, in order to determine the effect of a reduced number of shock-flame interactions in the phenomenon. The results from these simulations can be seen in Figures 18-20.

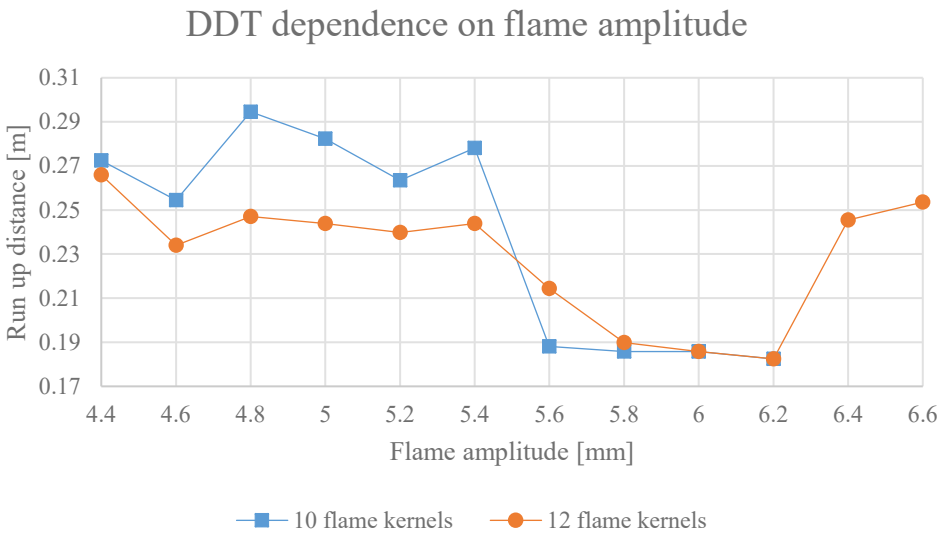

Figure 4.18: *DDT dependence on flame kernel amplitude for 10 and 12 flame kernels*

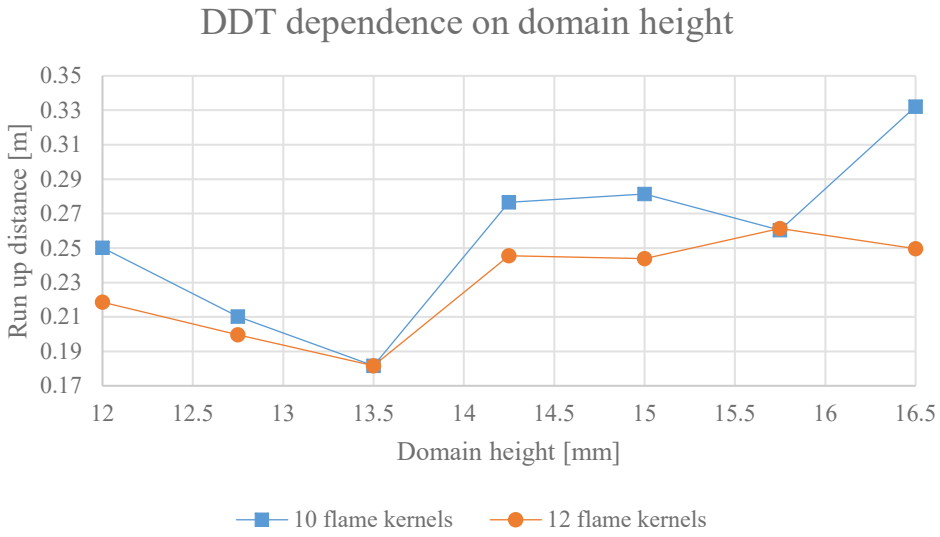

Figure 4.19: *DDT dependence on domain height for 10 and 12 flame kernels*

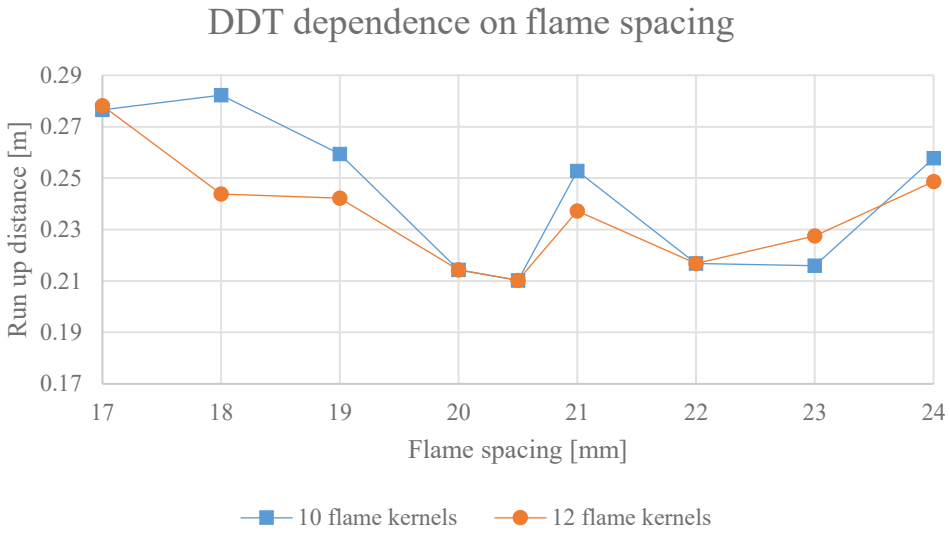

Figure 4.20: *DDT dependence on flame kernel spacing for 10 and 12 flame kernels*

As can be seen in figures, almost all 12 kernel simulations demonstrated equal or lower run up distance and time compared to the 10 kernels simulations. This difference of run up distance and onset time can also be seen in the temperature plots of Figure 4.21, which shows the onset of detonation for 10 and 12 kernel simulations and 16.5 mm domain height.

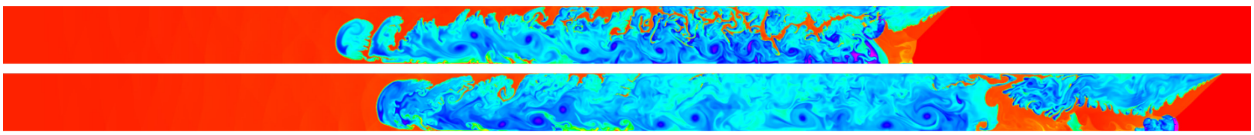

Figure 4.21: *Temperature plots at onset of detonation for 12 flame kernels (top) and 10 flame kernels (bottom)*

These results can be attributed to the effect that the increased number of interactions has on the deflagration speed, which is similar to the effect the number of obstructions has in a channel (Gamezo et al, 2008). More interactions result in more perturbations, which induce further mixing and therefore further acceleration of the flame brush. If the flame brush has accelerated sufficiently, then a shallower gradient can cause an explosion that will result to the formation of a detonation wave. For the 10 kernels simulations, ending the flame kernels sooner results to a rapid deceleration of the flame brush, since the large-scale flame folds burn out and new ones do not form. Therefore, an explosion is less likely to occur, since a steeper gradient of reactivity is required.

4.8 Summary

In order to assess the influence of various physical parameters on the transition event and to explore any scaling relationship among them, a parametric study is performed with a range of simulations considering varying domain size, ignited flame arrangements and initial conditions. Practically in real experiments, these parameters can be varied physically by controlling the ignition time and distance between each spark. The present study demonstrates that these aforementioned parameters can significantly control DDT and it is possible to optimize these parameters to achieve DDT at short run-up distance to obtain a self-propagation detonation.

Chapter 5

Conclusion

5.1 Concluding remarks

In this Thesis resolved 2-D Numerical simulations were obtained for a planar shock wave interacting with multiple flame kernels. The results of the simulations demonstrated that these interactions amplify the leading shock wave and accelerate the flame brush, resulting in a deflagration to detonation transition (DDT). As seen in the simulations, DDT is divided in four phases, the creation of the deflagration, the acceleration of the flame brush, the formation of explosion centers along with necessary amplification, and the final formation of detonation wave. For Navier-Stokes simulations, the acceleration of the flame brush is promoted by the intense turbulence generated through shock-flame and shock-boundary interactions. The explosion center develops ahead of the flame brush in the unreacted shocked material as a result of pressure wave reflections and coalescence and higher post shock temperatures near the top boundary. In the Euler simulations, although the flame acceleration and the formation of hot spot are affected by the suppression of turbulence and burning rate, DDT can still be achieved by the flow fluctuations generated through shock flame and shock boundary interactions. The explosion center for these simulations occurs later and further downstream compared to N-S simulations.

Finally, through a series of numerical simulations it was demonstrated that DDT is significantly affected when certain key parameters are modified. The parameters considered were the domain height, flame amplitude, flame spacing, number of flame kernels and incident shock speed. Modifying these parameters affects the acceleration process and the formation of hot spots, resulting in reduced run up distance and onset of detonation time for certain parameter values. The simulations with reduced incident shock speed also showed that a strong shock is not required for DDT, only the proper synchronization of the chemical energy release rate with the propagating shock wave.

5.2 Future work

Suggestions for continuation of this work involve modifying additional simulation parameters, such as flame temperature and activation energy, to determine their effect on DDT. For the domain, further modifications that could be examined include variable spacing between kernels and varying kernel diameter. Having varying kernel placements would allow to have denser placement for the initial shock-flame interactions in order to create more perturbations, increase the energy release rate and therefore accelerate the flame brush faster, and then place the following kernels further apart so that Mach stems can form and DDT can occur more easily. Different kernel sizing could aid in trapping or constraining unreacted material, therefore creating an explosion that would lead to the formation of the detonation wave. Finally, the current numerical framework should be further improved by using higher order schemes, inclusion of a turbulence model, use of a multiple step chemical kinetic model and higher resolution, which will allow to better resolve the boundary layers and turbulence. These modifications will inevitably increase the computational cost, therefore parallel CPU or GPU computing should also be explored to accelerate the simulation run-time.

References

1. Bach, G. G., Knystautas, R., & Lee, J. H. (1969) Direct initiation of spherical detonations in gaseous explosives. In *Symposium (international) on Combustion*. *12*(1): 853-864.
2. Bartenev, A.M. & Gelfand, B.E. (2000) Spontaneous initiation of detonations. *Prog. Energy Comb. Sci. 26*(1): 29-55.
3. Bates, K.R., (2005) *Numerical Simulation and Analysis of the Transition to Detonation in Gases*. PhD Thesis, University of Cambridge, UK
4. Berger, M. J. & Colella, P. (1989) Local adaptive mesh refinement for shock hydrodynamics. *J. Comput. Phys. 82*, 64-84
5. Berger, M. J. & LeVeque, R. J. (1998) Adaptive mesh refinement using wave- propagation algorithms for hyperbolic systems. *SIAM J. Numer. Anal. 35*, 2298-2316
6. Berger, M. J. & Oliger, J. (1984) Adaptive mesh refinement for hyperbolic partial differential equations. *J. Comput. Phys. 53*, 484-512
7. Bourlioux, A., Majda, A. J., & Roytburd, V. (1991). Theoretical and numerical structure for unstable one-dimensional detonations. *SIAM Journal on Applied Mathematics*, *51*(2), 303-343.
8. Ciccarelli, G. & Dorofeev, S. (2008) Flame acceleration and transition to detonation in ducts. *Prog. Combust. Sci. 34*(4): 499-550.
9. Erpenbeck, J. J. (1962) Stability of steady-state equilibrium detonations. *The physics of Fluids*, *5*(5): 604-614
10. Erpenbeck, J. J. (1964) Stability of idealized one-reaction detonations. *The Physics of Fluids*, *7*(5): 684-696
11. Fickett, W., & Davis, W. C. (1979). *Detonation*. University of California Press. Berkeley, CA.
12. Fickett, W., & Wood, W. W. (1966). Flow calculations for pulsating one-dimensional detonations. *Physics of Fluids*, *9* (5), 903-916.
13. Frolov, S.M. (2006) Initiation of strong reactive shocks and detonation by traveling ignition pulses. *J. Loss Prev. Proc. Ind. 19*: 238-244

14. Frolov, S.M., Basevich, V. Ya, Aksenov, V.S. & Polikhov, S.A. (2003) Detonation initiation by controlled triggering of electric discharges. *J. Prop. Power 19*(4): 573–580.
15. Gamezo, V. N., Ogawa, T., & Oran, E. S. (2008). Flame acceleration and DDT in channels with obstacles: effect of obstacle spacing. *Combustion and Flame*, *155*(1-2), 302-315.
16. Gamezo, V.N., Khokhlov, A.M. & Oran, E.S. (2001) The Influence of shock bifurcations on shock-flame interactions and DDT. *Combust. Flame 126*: 1810–1826.
17. He, L., & Lee, J. H. (1995) The dynamical limit of one-dimensional detonations. *Physics of Fluids*, *7*(5), 1151-1158.
18. Hern, S. D. (1999) *Numerical Relativity and Inhomogeneous Cosmologies*. PhD thesis, University of Cambridge, UK
19. Higgins, A.J., Pinard, P., Yoshinaka, A. & Lee, J.H.S. (2001) Sensitization of fuel-mixtures for deflagration to detonation transition. *High-Speed Deflagration and Detonation: Fundamentals and Control*, Elex-KM Publishers, Moscow, 2001, pp. 45-62.
20. Hwang, P., Fedkiw, R. P., Merriman, B., Aslam, T. D., Karagozian, A. R., & Osher, S. J. (2000) Numerical resolution of pulsating detonation waves. *Combust. Theory Modell.* 4: 217-240
21. Kailasanath, K. (2003) Recent developments in the research on pulse detonation engines. *AIAA J.* 41: 145–159.
22. Kapila, A.K., Schwendeman, D.W., Quirk, J.J. & Hawa, T. (2002) Mechanisms of detonation formation due to a temperature gradient. *Combust. Theory Modell. 6*: 553-594.
23. Kessler, D.A., Gamezo, V.N. & Oran, E.S. (2010) Simulations of flame acceleration and deflagration-to-detonation transitions in methane-air systems. *Combust. Flame 157*: 2063-2077.
24. Khokhlov, A.M. & Oran, E.S. (1999) Numerical simulation of detonation initiation in a flame brush: The role of hot spots. *Combust. Flame 119*: 400-416.
25. Khokhlov, A.M., Oran E.S. & Thomas, G.O. (1999) Numerical simulation of deflagration-to-detonation transition: the role of shock–flame interactions in turbulent flames. *Combust. Flame 117*(1-2): 323-339.
26. Khokhlov, A.M., Oran, E.S. & Wheeler, J.C. (1997) A theory of deflagration-to-detonation transition in unconfined flames. *Combust. Flame 108*: 503–517.

27. Kindracki, J., Kobiera, A., Wolanski, P., Gut, Z., Folusiak, M. & Swiderski, K. (2011) Experimental and numerical study of the rotating detonation engine in hydrogen-air mixtures. *Progress in Propulsion Physics 2*: 555-582.
28. Lee, J.H.S. (1977) Initiation of gaseous detonation. *Ann. Rev. Phys. Chem. 28*: 75-104.
29. Lee, J.H.S. (2008) *The Detonation Phenomenon*. Cambridge University Press, New York.
30. Lee, J.H.S. & Higgins, A.J. (1999) Comments on criteria for direct initiation of detonation. *Philos. Trans. R. Soc. A 357*(1764): 3503–3521.
31. Lee, J.H.S. & Moen, I.O. (1979) The mechanism of transition from deflagration to detonation in vapour cloud explosions. *Proc. Energy Comb. Sci. 6*: 359–389.
32. Middha, P. & Hansen, O.R. (2008) Predicting deflagration to detonation transition in hydrogen explosions. *Proc. Safety Prog. 27*(3): 192-204
33. Molkov V. (2012) Hydrogen Safety Engineering: The State-of-the-Art and Future Progress. In: *Comprehensive Renewable Energy.* (Eds: Sayigh, Ali), Elsevier, Oxford, pp. 77-109.
34. Ng, H.D. (2005). *The Effect of Chemical Reaction Kinetics on the Structure of Gaseous Detonations.* PhD Thesis, McGill University, Montreal, Canada
35. Ng, H.D. & Lee, J.H.S. (2003) Direct initiation of detonation with a multi-step reaction scheme. *J. Fluid Mech. 476*: 179-211.
36. Ng, H.D. & Lee, J.H.S. (2008) Comments on explosion problems for hydrogen safety. *J. Loss Prev. Proc. Indust. 21*(2): 136-146.
37. Nikiforakis, N. & Clarke, J.F. (1996a) Quasi-steady structures in the two-dimensional initiation of detonations. *ProcT. R. Soc. Lond. A 452*(1952): 2023-2042
38. Nikiforakis, N. & Clarke, J.F. (1996b). Numerical studies of the evolution of detonations. *Mathematical and Computer Modelling 24*(8): 149-164
39. Oran, E.S. (2015) Understanding explosions – From catastrophic accidents to the creation of the Universe. *Proc. Combust. Inst. 35*(1): 1-35.
40. Oran, E.S. & Gamezo, V.N. (2007) Origins of the deflagration-to-detonation transition in gas-phase combustion. *Combust. Flame 148*(1-2): 4-47.
41. Plewa, T. (1999) Adaptive mesh refinement for structured grids. (web page at http://www.camk.edu.pl/ ~tomek/AMRA/amr.html)

42. Roy, G.D., Frolov, S.M., Borisov, A.A. & Netzer, D.W. (2004) Pulse detonation propulsion: challenges, current status, and future perspective, *Prog. Energy Combust. Sci. 30*: 545-672.
43. Schultz, E., Wintenberger, E. & Shepherd, J.E. (1999) Investigation of deflagration to detonation transition for application to pulse detonation engine ignition systems. In: *Proceedings of the 16th JANNAF Propulsion Symposium*. Chemical Propulsion Information Agency.
44. Sharpe, G. J., & Falle, S. A. E. G. (1999). One-dimensional numerical simulations of idealized detonations. In *Proceedings of the Royal Society of London A: Mathematical, Physical and Engineering Sciences 455*(1983): 1203-1214.
45. Shepherd, J.E. (2009) Detonation in gases. *Proc. Combust. Inst. 32*(1):83-98.
46. Toro, E. F. (2006) *Riemann Solvers and Numerical Methods for Fluid Dynamics* (3rd ed.). Springer, Berlin
47. Toro, E. F., & Billett, S. J. (2000). Centred TVD schemes for hyperbolic conservation laws. *IMA Journal of Numerical Analysis*, *20*(1): 47-79.
48. Toro, E. F., Spruce, M., & Speares, W. (1994). Restoration of the contact surface in the HLL-Riemann solver. *Shock waves, 4*(1): 25-34.
49. Urtiew, P.A. & Oppenheim, A.K. (1966) Experimental observations of the transition to detonation in an explosive gas. *Proc. R. Soc. Lond. A* 295: 13–28.
50. Wolanski, P. (2013) Detonation propulsion. *Proc. Combust. Inst. 34*: 125-158.
51. Zel'dovich, Y. B., & Kompaneets, A. S. (1955). Theory of Detonation. State Publishing House of Technical and Theoretical Literature, Moscow.
52. Zel'dovich, Ya B., Librovich, V.B., Makhviladze, G.M. & Sivashinsky, G.I. (1970) On the development of detonation in a non-uniformly preheated gas. *Acta Astronautica 15*: 313–321.
53. Zhang, F. (Editor) (2012) *Shock Waves Science and Technology Library, Vol. 6: Detonation Dynamics*. Springer, Berlin Heidelberg.